Scaling laws for mixed-heated stagnant-lid convection and application to Europa

Frederic Deschamps[1] and Kenny vilella[2]

[1]Academia Sinica
[2]Hokkaido University

November 23, 2022

Abstract

Because rocks and ices viscosities strongly depend on temperature, planetary mantles and ice shells are often thought to be animated by stagnant-lid convection. Their dynamics is further impacted by the release of internal heat either through radioactive isotopes decay or tidal dissipation. Here, we quantify the impact of internal heating on stagnant-lid convection. We performed numerical simulations of convection combining strongly temperature-dependent viscosity and mixed (basal and internal) heating in 3D-Cartesian and spherical geometries, and used these simulations to build scaling laws relating surface heat flux, Φ_{surf}, interior temperature, T_{m}, and stagnant lid thickness, d_{lid}, to the system Rayleigh number, heating rate, H, and top-to-bottom viscosity ratio, $\Delta\eta$. These relationships show that T_{m} increases with H but decreases with $\Delta\eta$, while Φ_{surf} increases with H and $\Delta\eta$. Importantly, they also describe heterogeneously heated systems well, provided that the maximum dissipation occurs in hottest regions. For H larger than a critical value H_{crit}, the bottom heat flux turns negative and the system cools down both at its top and bottom. Two additional interesting results are that 1) while the rigid lid stiffens with increasing H, it also thins; and 2) H_{crit} increases with increasing $\Delta\eta$. We then use our scaling laws to assess the impact of tidal heating on Europa's ice shell properties and evolution. Our calculations suggest a shell thickness in the range 20-80 km, depending on viscosity and dissipated power, and show that internal heating has a stronger influence than the presence of impurities in the sub-surface ocean.

Scaling laws for mixed-heated stagnant-lid convection and application to Europa

Frédéric Deschamps[1] and Kenny Vilella[2]

[1] Institute of Earth Sciences, Academia Sinica, 128 Academia Road Sec. 2, Nangang, Taipei 11529, Taiwan.
[2] JSPS International Research Fellow, Hokkaido University, Sapporo, Japan.

Corresponding author: Frédéric Deschamps; email: frederic@earth.sinica.edu.tw

Submitted to *Journal of Geophysical Research Planets*
May 24th 2021, 42 pages, including 3 tables and 8 figures

Abstract. Because rocks and ices viscosities strongly depend on temperature, planetary mantles and ice shells are often thought to be animated by stagnant-lid convection. Their dynamics is further impacted by the release of internal heat either through radioactive isotopes decay or tidal dissipation. Here, we quantify the impact of internal heating on stagnant-lid convection. We performed numerical simulations of convection combining strongly temperature-dependent viscosity and mixed (basal and internal) heating in 3D-Cartesian and spherical geometries, and used these simulations to build scaling laws relating surface heat flux, Φ_{surf}, interior temperature, T_m, and stagnant lid thickness, d_{lid}, to the system Rayleigh number, heating rate, H, and top-to-bottom viscosity ratio, $\Delta\eta$. These relationships show that T_m increases with H but decreases with $\Delta\eta$, while Φ_{surf} increases with H and $\Delta\eta$. Importantly, they also describe heterogeneously heated systems well, provided that the maximum dissipation occurs in hottest regions. For H larger than a critical value H_{crit}, the bottom heat flux turns negative and the system cools down both at its top and bottom. Two additional interesting results are that 1) while the rigid lid stiffens with increasing H, it also thins; and 2) H_{crit} increases with increasing $\Delta\eta$. We then use our scaling laws to assess the impact of tidal heating on Europa's ice shell properties and evolution. Our calculations suggest a shell thickness in the range 20-80 km, depending on viscosity and dissipated power, and show that internal heating has a stronger influence than the presence of impurities in the sub-surface ocean.

Plain language summary. Convection is a mode of heat transfer that is thought to play or have played a key role in the cooling of planetary mantles and ice shells of icy bodies. The convection vigor, efficiency and ability to transport heat are all controlled by the properties of the systems in which it settles. In planetary mantles and ice shells, two important parameters are the variations of viscosity triggered by changes in temperature, which lead to the formation of a rigid lid at the top of the system, and the production of heat within the system, which weakens hot plumes rising from its base. In this article, we assess the combined effects of these two parameters. For this, we perform numerical simulations of convection, from which we deduce quantitative relationships between input and output parameters, the later including internal temperature and surface heat flux. We show that both heat flux and temperature increase with increasing internal heat production, while increasing the thermal viscosity contrast increases heat flux, but reduces temperature. We then apply our relationships to the case of Europa, a moon of Jupiter, and show that the thickness of its ice shell should be in the range 20-80 km.

Key points.

- We run simulations of stagnant-lid mixed-heated convection and build temperature and heat flux scaling laws from them
- Stagnant lid stiffens and thins with increasing rate of internal heating
- The critical rate of internal heating at which bottom heat flux turns negative increases with increasing viscosity ratio

1. Introduction

Heat transfer through planetary mantles and ice shells of large icy bodies is controlled by the properties of these systems. Due to the strong temperature-dependence of silicate rocks and ices viscosities, convection within these systems is likely to operate in the so-called stagnant-lid regime (*e.g.*, Christensen, 1984; Moresi and Solomatov, 1995), unless, as in the case of the Earth, specific conditions allow the development of plate tectonics. In stagnant-lid convection, a rigid layer forms at the top of the system as an extension of the top thermal boundary layer (TBL). Because this layer is not mobile and transports heat by conduction, its presence strongly alters heat transfer through the system. Another process altering the ability of convection to transfer heat towards the surface is the production of heat within the system. In systems heated both from their bases and their interiors, hot plumes rising from the bottom TBL get weaker with increasing rate of internal heating, and may not reach the surface if heat production is too high (*e.g.*, Travis and Olson, 1994; Deschamps et al., 2010a). As a result, the amount of heat that can be extracted from regions located beneath the system is reduced. Ultimately, for internal heating rate larger than a critical value, the bottom heat flux turns negative, meaning that the system cools down both from its top and its base. In rocky planets, a source of internal heating is the decay of long-lived radio elements (^{235}U, ^{238}U, ^{232}Th, and ^{40}K). Short-lived elements, mainly ^{26}Al, may have further played a role in the evolution of planetesimals, the parent bodies of rocky planets and asteroids. In the case of icy moons, tidal dissipation provides a source of heat within or at the bottom of the ice shell. The amount of heat released, and thus the evolution of the body, depends on its orbital properties and may vary with time (*e.g.*, Tobie et al., 2003, 2005; Roberts and Nimmo, 2008), with internal heating being null or negligible if the body is tidally locked or if it moves on a quasi-circular orbit. Quantifying the influence of internal heating on the ability of rocky mantles and ice shells to transport heat towards the surface is therefore essential to model accurately the long term evolution of icy bodies and rocky planets.

A convenient way to quantify these effects is to build relationships (or scaling laws) between the key parameters describing thermal evolution (mainly interior temperature and surface heat flux) and the system properties, for instance its rheology, Rayleigh number (which measures the vigor of convection and depends itself on the system physical and thermal properties), and rate of internal heating. Scaling laws may be built from series of numerical simulations of convection, in which one or more parameters are systematically varied. Here, we conduct such a study in the case of mixed-heated systems animated by stagnant-lid convection. In addition to building scaling laws, we parameterize the value of internal heating at which the bottom heat flux turns negative. Finally, we use our results to model the properties and evolution of Europa's outer ice shell.

2. Numerical model and simulations

We performed numerical simulations of thermal convection for an incompressible, infinite Prandtl number fluid using StagYY (Tackley, 2008). The fluid is heated both from the bottom and from within, and the internal heating is controlled by the heat production per unit of mass, H. The conservation equations of momentum, mass, and energy are then

$$\boldsymbol{\nabla}\bar{\bar{\sigma}} - \boldsymbol{\nabla}P = -\alpha\rho g T \boldsymbol{e_z} \quad (1)$$

$$\boldsymbol{\nabla}\cdot\boldsymbol{v} = 0 \quad (2)$$

and $$\rho C_P \frac{\partial T}{\partial t} = k\boldsymbol{\nabla}\cdot(\boldsymbol{\nabla}T) - \rho C_P \boldsymbol{v}\cdot\boldsymbol{\nabla}T + \rho H\ , \quad (3)$$

where the elements of the deviatoric stress tensor, $\bar{\bar{\sigma}}$, are $\sigma_{ij} = \eta\left(\partial v_i/x_j + \partial v_j/x_i\right)$, P is the non-hydrostatic pressure, $\boldsymbol{v}$ the velocity, T the temperature, $\boldsymbol{e_z}$ the radial unit vector, α, ρ, and C_P, and k the fluid thermal expansion, density, heat capacity and thermal conductivity (all assumed constant throughout the system), g the gravity acceleration, and η the fluid viscosity, which here varies with temperature. Numerical methods used to solve Eqs. (1) to (3) are detailed in Tackley (2008).

The geometry is either 3D-Cartesian or 3D-spherical. In this later case, the spherical shell is modelled with a set of Yin and Yang stripes (Kageyama and Sato, 2004), the shell curvature being controlled by the ratio between its inner and outer radii, $f = r_c/R$. Depending on the curvature and on the effective Rayleigh number, Ra_{eff} (defined below), the resolution of each Yin or Yang stripe varies between 192×576 and 512×1536 (corresponding to spherical grids of 384×768 to 1024×2048 points), and the radial resolution of the shell varies between 96 and 192 points. 3D-Cartesian simulations are performed in boxes with a horizontal to vertical aspect ratio equal to 4 in both x and y directions, and a grid resolution of 128×128×64 points for $Ra_{\mathrm{eff}} < 10^6$, 256×256×128 points for $10^6 \leq Ra_{\mathrm{eff}} < 10^8$, and 384×384×192 points for $Ra_{\mathrm{eff}} \geq 10^8$. In addition, for both 3D-Cartesian and 3D-spherical cases, the grid is vertically refined at the top and at the bottom of the domain. Overall, this provides a good sampling of plumes and thermal boundary layers, when they exist. The top and bottom boundaries are free slip and isothermal, and reflective boundary conditions are imposed on sidewalls of 3D-Cartesian simulations. In all cases, initial temperature distributions are built from random perturbations superposed on a 1D radial adiabatic profile with thin TBLs at top and bottom.

Conservation equations are non-dimensionalized with the characteristic properties of the system. Hereafter, non-dimensional quantities are distinguished from their dimensional forms by adding a tilde, ~. We used the thickness of the fluid layer, D, as characteristic length, and the super-adiabatic temperature jump across this layer, ΔT, as characteristic temperature. The non-dimensional temperature and internal heating rate are then given by $\tilde{T} = \left(T - T_{surf}\right)/\Delta T$, where T_{surf} is the surface temperature, and

$$\widetilde{H} = \frac{\rho H D^2}{k \Delta T}. \quad (4)$$

Non-dimentionalization further implies to replace the source term of momentum equation, $\alpha\rho gT$, by the Rayleigh number,

$$Ra = \frac{\alpha\rho g\Delta T D^3}{\eta\kappa}, \tag{5}$$

where $\kappa = k/\rho C_P$ is the thermal diffusivity. This number measures the ratio between buoyancy and viscous forces, and is an input parameter of our simulations.

The viscosity of ice strongly depends on temperature. Here, we modelled this dependency using the Frank-Kamenetskii (FK) approximation,

$$\eta = \eta_0 \exp\left[-a_\eta \frac{(T-T_0)}{\Delta T}\right], \tag{6}$$

where η_0 and T_0 are the reference viscosity and temperature, and a_η a parameter that controls the amplitude of viscosity variations. This approximation overestimates the surface heat flux by up to 30 % (*e.g.*, Reese et al., 1999), and it does not account for dependencies of viscosity on strain rate and grain size. Nevertheless, it facilitates the calculations and allows capturing the role of one specific parameter (here, internal heating), since a large number of FK simulations are available in the literature and can be used for comparisons. In the FK approximation, the non-dimensional viscosity, $\tilde{\eta} = \eta/\eta_0$, is given as a function of the non-dimensional temperature, $\tilde{T}$, by

$$\tilde{\eta} = \exp\left(-a_\eta \tilde{T}\right). \tag{7}$$

The top-to-bottom viscosity ratio, $\Delta\eta = \exp(a_\eta)$, is an input parameter of our simulations. For viscosity ratios larger than 10^4, convection generally operates in the so-called stagnant-lid regime (*e.g.*, Christensen, 1984; Davaille and Jaupart, 1993; Moresi and Solomatov, 1995), in which a highly viscous (stagnant) lid develops at the top of the fluid. In this layer, heat is transported by conduction, thus reducing the heat transfer. Experimental rheological laws for ice Ih (Durham et al., 2010) imply that the top-to-bottom viscosity ratios through the outer ice shells of icy bodies are much larger than 10^4. Convection within these shells, if occuring, should then operate in the stagnant-lid regime.

In most cases, we assumed homogeneous heating, *i.e.*, H is constant throughout the system. Tidal dissipation within icy bodies may however depends on viscosity (Tobie et al., 2005), which, in our simulations, varies with temperature. We therefore calculated a few cases with viscosity-dependent internal heating. Following Roberts and Nimmo (2008), we assumed that internal heating is given by

$$H = H_0 \left[\frac{\omega\eta/\mu}{1+(\omega\eta/\mu)^2}\right] \Big/ \left[\frac{\omega\eta_{ref}/\mu}{1+\left(\omega\eta_{ref}/\mu\right)^2}\right] \qquad (8)$$

where η_{ref} and μ are the reference viscosity and rigidity of ice, H_0 a constant, and ω the orbital frequency. Note that the reference viscosity in Eq. (8) may be different from that defined in Eq. (6), provided that in calculations a correction is applied for consistency. Here, because we assumed that the strongest dissipation occurs close to the melting point of ice, η_{ref} is defined at the bottom of the ice shell (*i.e.*, for $\tilde{T} = 1$). In Eq. (6), by contrast, the reference viscosity η_0 is the surface viscosity (for $\tilde{T} = 0$), which implies $\eta_{ref} = \eta_0 \exp\left(-a_\eta\right)$. The non-dimensional internal heating rate may then be written

$$\tilde{H} = \tilde{H}_0 \left[\frac{\zeta_{ref}\tilde{\eta}\exp(a_\eta)}{1+\left(\zeta_{ref}\tilde{\eta}\exp(a_\eta)\right)^2}\right] \Big/ \left[\frac{\zeta_{ref}}{1+\zeta_{ref}^{\,2}}\right] \qquad (9)$$

where $\zeta_{ref} = \omega\eta_{ref}/\mu$ and $\tilde{\eta}$ is given by Eq. (7). The viscosity at which dissipation is maximal depends on the exact value of ζ_{ref}. With μ around 4.0×10^9 Pa, orbital period of a few hours to a few days (corresponding to ω in the range 3.0×10^{-5}-3.0×10^{-6} s^{-1}), and $5.0\times10^{12} \leq \eta_{ref} \leq 5.0\times10^{14}$ Pas, ζ_{ref} may be chosen in the range 4.0×10^{-3}-4.0. Here, we fixed ζ_{ref} to 1, so that the maximum dissipation occurs exactly at η_{ref}. This further implies that dissipation is strongest in hottest regions, including plumes heads, as done in Tobie et al. (2003).

Because in our simulations viscosity varies throughout the system, the definition of the Rayleigh number, *Ra* (Eq. 5), is ambiguous. The input *Ra* can however be defined at a specific viscosity (or equivalently, a specific temperature), such that it does not vary during the simulations. Here, we prescribed the surface Rayleigh number, Ra_{surf}, defined from the surface viscosity and temperature. In stagnant-lid convection, a better description of the vigor of convection beneath the lid is given by the effective Rayleigh number, Ra_{eff}, calculated with the viscosity at the temperature of the well-mixed interior (or interior temperature), $\tilde{T}_m$, which is defined as the volume averaged temperature within the adiabatic region. Following Eqs. (6) and (8), Ra_{eff} is given by

$$Ra_{eff} = Ra_{surf} \exp\left(a_\eta \tilde{T}_m\right) . \tag{10}$$

Note that $\tilde{T}_m$, and thus Ra_{eff}, are outputs of the simulations.

A key output observable is the amount of heat transported to the surface, measured with the heat flux. In mixed-heated systems, the conservation of energy implies that its top and bottom values, Φ_{top} and Φ_{bot}, satisfy

$$\Phi_{top} = f^2 \Phi_{bot} + \frac{\left(1+f+f^2\right)}{3} H , \tag{11}$$

where *f* is the ratio between the inner and outer shell radii, equal to 1 in Cartesian geometry. The characteristic heat flux is defined as the conductive heat flux for pure basal heating in Cartesian geometry, $\Phi_{carac} = k\,\Delta T/D$, such that the non-dimensional form of Eq. (11) is simply obtained by replacing each variable by its non-dimensional equivalent, $\tilde{\Phi}_{top}$, $\tilde{\Phi}_{bot}$ and $\tilde{H}$. Equation (11) indicates that, for a given Φ_{top}, the production of heat within the system lowers the amount of heat that can be extracted from regions located below (for instance, planetary cores). If internal heating is too large, the system cannot extract heat from the bottom but cools down both from its top and its bottom (*e.g.*, Moore 2008; Vilella and Deschamps, 2018), meaning that Φ_{bot} is negative. It is useful to introduce the Urey ratio, measuring the ratio between the internal heat production and the surface heat flux,

$$Ur = \frac{(1+f+f^2)}{3} \frac{H}{\Phi_{top}} . \quad (12)$$

Eqs. (11) and (12) imply that $Ur > 1$ if Φ_{bot} is negative, and $0 \leq Ur \leq 1$ otherwise.

Convection operates only if the convective heat flux is larger than the conductive heat flux Φ_{cond}, which, for a mixed heated system, depends on depth (Table S1). Its surface expression is given by

$$\Phi_{cond,top} = f \frac{k\Delta T}{D} + (f+2) \frac{\rho H D}{6} , \quad (13)$$

whose non-dimensional form (with respect to the characteristic heat flux) writes

$$\widetilde{\Phi}_{cond,top} = f + \frac{(f+2)}{6} \widetilde{H} . \quad (14)$$

The efficiency of heat transfer is measured with the Nusselt number, Nu, defined as the ratio between the convective and conductive heat flux. Convection operates if $Nu > 1$. As an example, in Cartesian geometry ($f = 1$), $Nu > 1$ requires that the surface non-dimensional convective heat flux, $\widetilde{\Phi}_{top}$, is larger than $\left(1 + \widetilde{H}/2\right)$.

Using this setup, we performed 63 simulations in 3D-Cartesian geometry (including 9 cases with heterogeneous heating) and 25 in 3D-spherical geometry (Table 1). For comparison, we also listed 5 cases with pure bottom heating taken from Deschamps and Lin (2014). Surface Rayleigh number, top-to-bottom viscosity ratio, and non-dimensional heating rate are taken in the ranges $1 \leq Ra_{surf} \leq 180$, $10^4 \leq \Delta\eta \leq 10^8$, and $0.5 \leq \widetilde{H} \leq 10$ respectively, leading to effective Rayleigh numbers between 2.0×10^5 and 2.0×10^8. In 3D-spherical cases, the inner-to-outer radii ratio is chosen between 0.6 and 0.85. For these ranges of values, the flow is time-dependent and reaches a quasi-stationary state (meaning that output properties, including $\tilde{T}_m$ and $\widetilde{\Phi}_{top}$, oscillate around constant values) after some time. Output properties are estimated after the quasi-stationary phase has been reached, by time-averaging of each property over several oscillations.

3. Flow pattern and thermal structure

3.1 Flow pattern

Stagnant-lid convection appears for top-to-bottom viscosity ratios larger than 10^4 (Moresi and Solomatov, 1995), but its occurrence requires larger viscosity contrasts as the Rayleigh number (Deschamps and Sotin, 2000) or shell curvature (Yao et al., 2014; Guerrero et al., 2018) increases. Stein et al. (2013) proposed two criteria to assess the presence of a stagnant lid. First, a non-dimensional surface velocity, $\tilde{v}_{surf}$, lower than 1; and second a mobility, M, defined as the ratio between $\tilde{v}_{surf}$ and the root mean square velocity of the whole system, smaller than 0.01. All our simulations satisfy these criteria (Table 1), and should thus belong to the stagnant-lid regime.

Figures 1 to 3 show snapshots of temperature fields and associated horizontally averaged profiles for 3D-Cartesian cases with same surface Rayleigh number (Ra_{surf} = 25) and viscosity ratio ($\Delta\eta = 10^6$), but different rates of internal heating, and for 3D-spherical cases with f = 0.6, Ra_{surf} = 16, $\Delta\eta = 10^6$ and, again, different values of $\widetilde{H}$. A stagnant lid is clearly visible in all cases. A closer examination (section 3.2) indicates that the lid is thinning with increasing $\widetilde{H}$. Internal heating has a strong impact on the flow structure beneath the lid. With increasing $\widetilde{H}$, we observe a trend similar to that reported for isoviscous fluids (*e.g.*, Travis and Olson, 1994; Deschamps et al., 2010a). Plumes are getting thinner, more diffuse and may not reach the bottom of the stagnant lid, indicating that the growth of hot instabilities in the base thermal boundary layer (TBL) is more difficult. The flow is progressively controlled by downwellings and return flow. Importantly, if $\widetilde{H}$ is large enough (Figs. 1g-h, and 2c-d), the bottom TBL disappears and the heat flux turns negative (Figure 3d and 3f). The system then cools down both at its top and its bottom, and the Urey ratio (Eq. 12) is larger than 1.

3.2 Properties of the stagnant lid

We measured the (non-dimensional) thickness of the stagnant lid, $\tilde{d}_{lid}$, using the method developed by Davaille and Jaupart (1993), in which the base of the stagnant lid is defined by the intersection between the tangent at the point of inflexion of the horizontally averaged profile of vertically advected heat, $\tilde{v}_z\tilde{T}$, with the origin axis ($\tilde{v}_z\tilde{T} = 0$; left plots in Figure 3). The values of $\tilde{d}_{lid}$ we obtained are reported in Table 1. All other parameters being equal, $\tilde{d}_{lid}$ decreases with increasing rate of internal heating, while both $\tilde{v}_{surf}$ and M are decreasing. Increasing internal heating thus results in thinner but stronger stagnant lids.

Because heat is transported by conduction in the stagnant lid, it is possible to derive analytical expressions for the horizontally averaged temperature in this region by solving the conduction heat equation. Assuming that internal heating rate and density are constant and that the surface temperature and heat flux (T_{surf} and Φ_{surf}) are known, the (dimensional) temperature profile is given either by Eq. (S7) in Cartesian geometry, or Eq. (S8) in spherical geometry of (Supporting Information, SI). Note that these expressions are independent of the lid thickness. Their non-dimensional forms are

$$< \tilde{T} >= \tilde{z}\tilde{\Phi}_{top} - \frac{\tilde{H}}{2}\tilde{z}^2 \tag{15}$$

where $\tilde{z}$ is the non-dimensional depth, and

$$< \tilde{T} >= -\frac{\tilde{\Phi}_{top}}{(1-f)}\left[1 - \frac{\tilde{R}}{\tilde{r}}\right] + \frac{\tilde{H}}{6(1-f)^2}\left[2\left(1 - \frac{\tilde{R}}{\tilde{r}}\right) + \left(1 - \frac{\tilde{r}^2}{\tilde{R}^2}\right)\right], \tag{16}$$

where $\tilde{r} = (1-f)^{-1} - \tilde{z}$ and $\tilde{R} = (1-f)^{-1}$ are the non-dimensional radius and total radius, respectively. Solving heat equation for viscosity-dependent internal heating is more complex in the general case. In our case, however, imposing the maximum dissipation at lowest viscosity implies that dissipation in the lid is close to zero. A good description of the temperature profile within the lid is then obtained by setting $\tilde{H} = 0$ in Eqs. (15) and (16).

The horizontally averaged heat flux within the stagnant lid is given by Eqs. (S11) and (S12) of SI, whose non-dimensional versions are

$$\widetilde{\Phi}(\tilde{z}) = \frac{\tilde{T}_{lid}}{\tilde{d}_{lid}} + \frac{\tilde{H}}{2}\left(\tilde{d}_{lid} - 2\tilde{z}\right) \tag{17}$$

and

$$\widetilde{\Phi}(\tilde{z}) = \frac{\tilde{T}_{lid}}{\tilde{d}_{lid}} f_{lid} \frac{\tilde{R}^2}{\tilde{r}^2} - \frac{\tilde{H}}{6(1-f)}\left[f_{lid}(1+f_{lid})\frac{\tilde{R}^2}{\tilde{r}^2} - 2\frac{\tilde{r}}{\tilde{R}}\right], \tag{18}$$

where $\tilde{d}_{lid}$ and $\tilde{T}_{lid}$ are the non-dimensional stagnant lid thickness and basal temperature, respectively, and $f_{lid} = (R - d_{lid})/R = 1 - (1-f)\, d_{lid}/D$ is the ratio between the radius of its base and the total radius. To obtain Eq. (18), it is useful to recall that $\tilde{R} = (1-f)^{-1}$. Equations (17) and (18) can be used to estimate the temperature at the bottom of the lid as a function of the surface heat flux and stagnant lid thickness. Setting $\tilde{z} = 0$ in Eq. (17) and $\tilde{r} = \tilde{R}$ in Eq. (18), and re-arranging the terms leads to

$$\tilde{T}_{lid} = \tilde{d}_{lid}\left(\widetilde{\Phi}_{top} - \frac{1}{2}\tilde{H}\tilde{d}_{lid}\right) \tag{19}$$

in Cartesian geometry, and

$$\tilde{T}_{lid} = \frac{\tilde{d}_{lid}}{f_{lid}}\left[\widetilde{\Phi}_{top} - \frac{1}{6}\tilde{H}\frac{\left(2 - f_{lid} - f_{lid}{}^2\right)}{(1-f)}\right] \tag{20}$$

in spherical geometry. Values of $\tilde{T}_{lid}$ deduced either from Eq. (19) or Eq. (20) are reported in Table 1.

To check the validity of our approach, we inserted the values of $\tilde{d}_{lid}$ we measured (Table 1) and the values of $\tilde{T}_{lid}$ calculated by Eqs. (19) and (20) in Eqs. (15) and (16), respectively. This provides an excellent description of the top part of the horizontally averaged temperature profiles, corresponding to the stagnant lid (dashed dark red curves in Fig. 3). Note that the values of $\tilde{T}_{lid}$ obtained with Eq. (19) or Eq. (20) are slightly larger than that measured on the horizontally averaged profiles of temperature.

4. Scaling laws

Reconstructing potential thermal evolutions of planets and satellites with parameterized convection methods requires the knowledge of appropriate relationships between input parameters (Rayleigh number, viscosity ratio, and rate of internal heating) and observables (interior temperature, surface heat flux, stagnant lid thickness), or scaling laws for short. Results from our numerical simulations allow us to build such scaling laws. These are detailed below and summarized in Table 2.

4.1 Temperature of the well-mixed interior

Numerical simulations indicate that the interior temperature of an isoviscous, mixed-heated fluid is well described by a relationship combining the interior temperature for pure bottom and pure internal heating (Sotin and Labrosse, 1999; Deschamps et al., 2010a). Here, we followed a similar approach and built a scaling that combines the interior temperature for a bottom-heated fluid animated by stagnant-lid convection (Deschamps and Lin, 2014; Yao et al., 2014), and for an internally-heated fluid, leading to

$$\tilde{T}_m = 1 - \frac{a_1}{f^{a_2}\gamma} + (c_1 + c_2 f)\left[\frac{(1+f+f^2)}{3}\tilde{H}\right]^{c_4}\frac{1}{Ra_{eff}{}^{c_3}}, \qquad (21)$$

where parameters a_1, a_2 and c_1 to c_4 can be obtained by inversion of the $\tilde{T}_m$ predicted by simulations (Table 1), and $\gamma = \Delta T/\Delta T_v$ is the non-dimensional inverse of the viscous temperature scale, ΔT_v, defined as

$$\Delta T_v = \left(-\frac{1}{\eta}\frac{d\eta}{dT}\Big|_{T=T_m}\right)^{-1}. \qquad (22)$$

In the case of Frank-Kamenetskii approximation (Eq. 6), $\gamma = a_\eta = \ln(\Delta\eta)$. For consistency with scaling laws obtained for pure bottom heating, we fixed a_1 and a_2 to the values obtained by Yao et al. (2014), $a_1 = 1.23$ and $a_2 = 1.5$. We then performed two separate inversions, for $Ur < 1$ and

Ur > 1, in which we excluded simulations with heterogeneous heating. The inversion method follows the generalized inversion method of Tarantola and Valette (1982), and we assumed relative uncertainties of 0.5 % on observed $\tilde{T}_m$, accounting for the time-variations of this observable during the steady-state phase. For Ur < 1, the best fitting values are c_1 = 4.3, c_2 = -2.8, c_3 = 0.26 and c_4 = 0.96, with a chi-square of 20 (the total number of experiments used for this inversion being 46). The value of c_3 is fairly close to the theoretical value of the Rayleigh number exponent for a purely internally heated fluid, 0.25 (Parmentier and Sotin, 2000). We therefore did an additional inversion in which we fixed c_3 to 0.25, and (for simplicity) c_4 to 1.0, and found c_1 = 3.5 ± 0.12 and c_2 = -2.3 ± 0.11, still with a good chi-square, around 30. We followed a similar procedure for Ur > 1 (28 simulations). In that case, the best fit is obtained for c_1 = 4.5, c_2 = -3.1, c_3 = 0.34 and c_4 = 1.75. Fixing, for simplicity, c_3 to 1/3, we obtained c_1 = 4.4 ± 0.22, c_2 = -3.0 ± 0.17, and c_4 = 1.72 ± 0.02, with a chi-square of 39. Figure 4a compares modelled and observed values of $\tilde{T}_m$. Note that the calculations with heterogeneous heating, which were all conducted with Ur < 1 but were not included in the inversion process, are well described by the scaling law for Ur < 1.

Because the effective Rayleigh number, Ra_{eff}, depends on $\tilde{T}_m$, solving Eq. (21) for $\tilde{T}_m$ requires the use of a zero-search method. As a consequence, identifying trends in the variations of $\tilde{T}_m$ with the input model parameters (surface Rayleigh number, rate of internal heating, thermal viscosity ratio, and curvature) is not straightforward. However, a close examination of Table 1 indicates that, other parameters being fixed, $\tilde{T}_m$ increases with $\widetilde{H}$ and f, but decreases with Ra_{surf}. Changes of $\tilde{T}_m$ with $\Delta\eta$ are more complex (Figure S2a). For $\widetilde{H}$ around 0.5-1.0 and higher, $\tilde{T}_m$ first decreases with increasing $\Delta\eta$, reaches a minimum for a value of $\Delta\eta$ that increases with $\widetilde{H}$, and then starts increasing again. For $\widetilde{H} < 1$, $\tilde{T}_m$ increases monotonically with $\Delta\eta$, as observed for purely bottom heated convection. Figures S1 and S2, built from Eq. (21)

further illustrate these trends. Interestingly, for the range of γ expected in ice layers, around 15-20 (section 5.1), and $\widetilde{H} > 1$ one expects $\tilde{T}_m$ to decrease with increasing viscosity ratio.

4.2 Surface heat flux

Heat flux through thermal boundary layers (TBL) scales as a power law of the Rayleigh number and of the temperature jump across the TBL (*e.g.*, Moore and Weiss, 1973), implying that in stagnant-lid convection it also scales as the temperature viscous scale. The horizontally averaged non-dimensional surface heat flux may then be written as a function of the Rayleigh number and of the parameter γ (section 4.1), which is, again, equal to ln(Δη) in the case of the Frank-Kamenetskii approximation. Figure 4b shows that regardless of $\widetilde{H}$, the surface heat flux observed in our simulations with *Ur* < 1 is very well described by the scaling obtained by Deschamps and Lin (2014) and may thus be written

$$\widetilde{\Phi}_{top} = a\frac{Ra_{eff}{}^{b}}{\gamma^{c}}, \tag{23}$$

where Ra_{eff} is the effective Rayleigh number (Eq. 10), and the constants *a*, *b*, and *c* are equal to 1.46, 0.27, and 1.21, respectively. Spherical cases for *Ur* < 1 also fit well along this parameterisation, and do not require small correction for *f*, as suggested by Yao et al. (2014). A reappraisal of Yao et al. (2014) calculations further shows that for *f* > 0.6 such a correction is not needed. Note that $\widetilde{\Phi}_{top}$ implicitly depends on *f* through Ra_{eff}, which increases with interior temperature $\tilde{T}_m$. Because $\tilde{T}_m$ decreases with *f*, $\widetilde{\Phi}_{top}$ also decreases with increasing curvature. Interestingly, heat fluxes observed in cases with heterogeneous heating are slightly lower than those predicted by our scaling, but still fit very well along it, suggesting that the distribution of heat within the system does not substantially affect the surface heat flux. For *Ur* > 1, our calculations indicate that $\widetilde{\Phi}_{top}$ also fits well along Eq. (23) with *a* = 1.57 and values of *b* and *c* similar to those for *Ur* < 1 (Figure 4b). Finally, the bottom heat flux, $\widetilde{\Phi}_{bot}$, can easily be calculated by inserting Eq. (23) in the non-dimensional version of Eq. (11).

While increasing $\widetilde{H}$ results, of course, in larger $\widetilde{\Phi}_{top}$ and smaller $\widetilde{\Phi}_{bot}$, the influence of the thermal viscosity ratio, $\Delta\eta$, on $\widetilde{\Phi}_{top}$ is less intuitive. The $1/\gamma^c$ term and, if γ is not too high, the decrease of $\tilde{T}_m$, both lower $\widetilde{\Phi}_{bot}$ as $\Delta\eta$ increases. However, the exponential term in the definition of Ra_{eff} (Eq. 10) remains dominant, such that for given values of Ra_{surf} and $\widetilde{H}$, $\widetilde{\Phi}_{top}$ increases with increasing $\Delta\eta$ (Figure S2). An interesting consequence is that the Urey ratio (Eq. 12) decreases with increasing thermal viscosity ratio, as also shown in Table 1. In other words, given the properties (thickness, density, thermal expansion and diffusivity, super-adiabatic temperature jump, gravity acceleration, and rate of internal heating) of a mixed-heated shell animated by stagnant-lid convection, increasing viscosity ratio allows the system to extract more heat from the underlying layer (*i.e.*, the bottom heat flux increases). This somewhat counter-intuitive feature results from the strong increase in Ra_{eff} with increasing $\Delta\eta$, implying that convection in the well-mixed interior gets more vigorous.

4.3 Transition between positive and negative bottom heat flux

If internal heating is too large, convection cannot evacuate all the heat produced towards the surface. A fraction of this heat is released at the base of the system, resulting in a negative bottom heat flux, $\widetilde{\Phi}_{bot}$. Setting $\widetilde{\Phi}_{bot} = 0$ in Eq. (12) provides a criterion for the maximum amount of internal heat that can be transported to the surface as a function of the system properties (Rayleigh number, curvature, and viscosity ratio),

$$\widetilde{H}_{crit} = \frac{3a}{(1+f+f^2)\gamma^c} {Ra_{eff}}^b \qquad (24)$$

Again, because Ra_{eff} depends implicitly (through $\tilde{T}_m$) on $\widetilde{H}$, Eq. (24) does not have analytical solutions, but can be solved with a zero search method. An additional difficulty in estimating

$\widetilde{H}_{crit}$ is that, while the scalings obtained for *Ur* < 1 and *Ur* > 1 overlap at $\widetilde{\Phi}_{bot} = 0$ within the error bars on scaling parameters values, they are not continuous when using the average values of these parameters (Table 2). A simple solution to this problem is to first calculate threshold values of $\widetilde{H}$ with both *Ur* < 1 and *Ur* > 1 scalings, $\widetilde{H}_{crit}^{-}$ and $\widetilde{H}_{crit}^{+}$, respectively, and second to define the value of $\widetilde{H}_{crit}$ as the average of these two bounds.

We then solved Eq. (24) for Ra_{surf} in the range 0.3-300, Δη in the range 10^4-10^8, and f between 1 (Cartesian geometry) and 0.6, and found that $\widetilde{H}_{crit}$ is well described by

$$\widetilde{H}_{crit} = \frac{3}{(1+f+f^2)} a_H \exp(c_H \gamma) Ra_{surf}^{b_H}, \tag{25}$$

where $a_{\mathrm{H}} = 0.184$, $b_{\mathrm{H}} = 0.31$, and $c_{\mathrm{H}} = 0.19$. Equation (25) provides a convenient way to estimate $\widetilde{H}_{crit}$ and is in good agreement with our numerical simulations (Figure 5). It shows that $\widetilde{H}_{crit}$ increases with Ra_{surf}, Δη, and curvature (decreasing *f*). Note that rescaling Eq. (25) implies to multiply each of its member by $k\Delta T/\rho D^2$ (Eq. 4). Because Ra_{surf} is proportional to D^3, one expects the dimensional critical heating rate, H_{crit}, to decrease approximately as 1/*D*. Thus, the transition to a negative heat flux is reached for lower heating rates in thick layers than in thin layers, unless the thermal viscosity ratio and/or the super-adiabatic temperature jump increase dramatically with *D*.

Finally, an interesting result is that, because $\widetilde{\Phi}_{bot}$ increases with the thermal viscosity ratio Δη (section 4.2), $\widetilde{H}_{crit}$ also increases with Δη. Therefore, given the properties of a mixed-heated shell animated by stagnant-lid convection, increasing Δη allows the system to extract heat from the underlying core up to higher rate of internal heating.

4.4 Thickness of the stagnant lid

Following Eqs. (15) and (16), the temperature profile within the lid is not a linear function of depth. However, Figure 3 suggests that these profiles are, at first order, well described by a linear function. This, in turn, implies that the thickness of this lid should approximately scales as the inverse of the heat flux, leading to

$$\tilde{d}_{lid} = a_{lid} \frac{\gamma^c}{{Ra_{eff}}^b}, \tag{26}$$

where the values of parameters b and c are identical to those for surface heat flux (b = 0.27 and c = 1.21), and a_{lid} is a constant. Figure 4c shows that Eq. (26) provides a good description of the stagnant lid thickness, with best fit to the measured stagnant lid thicknesses obtained for a value of a_{lid} = 0.633 ± 0.03 for Ur < 1, and a_{lid} = 0.667 ± 0.01 for Ur > 1.

5. Application to Europa

We now use the results obtained in section 4 to estimate the properties and thermal evolution of Europa outer ice shell. Our purpose is not to provide a detailed description of Europa's evolution, since we do not consider time-dependent internal heating based on Europa's orbital evolution, but instead to assess quantitatively the role played by tidal heating within the ice layer. This approach can easily be extended to other bodies, including Pluto, which is today tidally locked but may have experienced tidal heating early in its history.

A feature common to many (if not all) large icy bodies of the outer solar System is the persistence of a sub-surface ocean beneath an outer ice Ih shell (*e.g.*, Hussmann et al., 2007). In the case of Europa the presence of a sub-surface ocean is supported by anomalies in its external magnetic field, attributed to an internal magnetic field induced within a sub-surface liquid layer (Khurana et al., 1998). Europa's average density suggests that its rocky core is large, ~ 70 % in volume, corresponding to a radius of ~ 1400 km. Given Europa's gravity acceleration, 1.31 m/s^2, the pressure at the surface of the core is not large enough to allow the presence of high pressure ices. Europa's radial structure therefore likely consists of a large rocky core, surrounded by a liquid layer composed of water and impurities, and an outer ice layer. The exact nature of impurities is still debated. Present species may include salts, in particular magnesium sulfate ($MgSO_4$) (Vance et al. 2018), and volatile compounds such as ammonia (NH_3), methanol (CH_3OH), and methane (CH_4), which are all predicted to condensate in giant planets environments with amounts up to a few per cent (*e.g.*, Mousis et al., 2009; Deschamps et al., 2010b). The presence of impurities acts as an anti-freeze, opposing or delaying the crystallization of the sub-surface ocean. Interestingly, while the exact nature of impurities may affect the sub-surface ocean physical properties, including its density, it does not qualitatively impact the crystallization process, *i.e.*, different species present in different amounts would lead to similar evolution. For instance, Vilella et al. (2020) pointed out that the impact of 30 % $MgSO_4$ on the liquidus is equivalent to that of 3.5 % NH_3.

Our modelling approach is detailed in SI. It is mostly similar to the one used in Deschamps (2021a), except for the treatments of the interior temperature, T_m, and of the stagnant lid thickness, d_{lid}. Another important difference is that two sets of parameters are used to calculate T_m and the surface heat flux, Φ_{surf}, depending on whether the bottom heat flux, Φ_{bot}, is positive ($Ur < 1$) or negative ($Ur > 1$) (Table 2). Note that instead of solving Eq. (25) to decide which set of parameters to use, we apply a simpler procedure, which accounts for the fact that temperature and heat flux scalings are not continuous at $Ur = 1$. First, we calculate T_m and Φ_{surf} assuming parameter values for $Ur < 1$. If the corresponding Φ_{bot} calculated with Eq. (11) is negative, we calculate T_m and Φ_{surf} again, but with parameter values for $Ur > 1$. If the resulting Φ_{bot} turns back to positive, we set arbitrarily its value to zero and recalculate Φ_{surf} and T_m accordingly.

Physical properties of Europa and ice Ih used for calculations are listed in Table 3, and we considered two possible initial compositions for the subsurface ocean, pure water and a mix of water and ammonia. In this later case, we fixed the initial amount of ammonia, x_{NH3}^{init}, to 3.0 vol%, corresponding to about 2.2 wt%. This value may be considered as an upper (possibly exaggerated) bound, and we chose it to obtain a conservative estimate of the impact of impurities on the ice shell properties and evolution. Concentration in ammonia then increases as the ice layer thickens, since only water crystalizes, while impurities are left in the sub-surface ocean. The reference viscosity, η_{ref}, is taken as a free parameter and varied between 10^{12} and 10^{15} Pas, a range extended from Montagnat and Duval (2000) estimates of polar ice sheet flow. Results are presented either for a given rate of heating per mass unit, H, or a given total power dissipated in the ice shell, P_{tide}. For an ice shell thickness D_{ice}, H and P_{tide} are related by (see also Figure S3)

$$H = \frac{3P_{tide}}{4\pi R^3\left[1-\left(1-\frac{D_{ice}}{R}\right)^3\right]}, \tag{27}$$

where R is the total radius of Europa.

5.1 Ice shell properties

As heat dissipation in the ice shell increases, two transitions may occur. First, at heating rate H_{crit} the heat flux at the bottom of the shell may turn negative, heating up the underlying sub-surface ocean and delaying its crystallization. Convection can still operate within the shell, but would be driven by downwellings and described with scaling laws for $Ur > 1$ (section 4). Second, at heating rate H_{melt} the bottom temperature exceeds the water liquidus, triggering melting at the bottom of the shell. This implies that the ice shell cannot be thicker than a critical value, D_{melt}. Local pockets of partial melt may further appear in hottest regions (plumes head), introducing additional complexities that are not accounted for by our modelling (see Vilella et al., 2020 for a discussion on this topic). Here, we estimate H_{melt} by comparing the liquidus of pure water with the ice shell horizontally averaged temperature, which underestimates the presence of local pockets of melt. However, because the inverse of the non-dimensional viscous temperature scale γ, which is here equal to $E\Delta T/RT_m{}^2$ (SI), is somewhat high, this bias should be limited (Vilella et al., 2020). Figure 6 shows that both H_{crit} and H_{melt} decrease with increasing ice layer thickness, D_{ice}. The decrease in H_{crit} is mostly related to the thickening of the ice layer (section 4.3). The decrease in H_{melt} is a consequence of the water liquidus, which is itself decreasing with depth, thus favoring partial melting at lower heating rates. In other words, D_{melt} decreases with increasing H. Taking $H = 10^{-9}$ W/kg and a reference viscosity $\eta_{ref} = 10^{14}$ Pas, for instance, D_{melt} is around 45 km, corresponding to a total power of ~ 1.2 TW. Figure S4 further indicates that all other parameters being the same, D_{melt} decreases with increasing η_{ref}. As one would expect, in the case of a pure water ocean H_{crit} is very close to H_{melt}. It is also worth noting that the addition of ammonia in the sub-surface ocean moderates the effects of H, allowing slightly thicker ice shells at a given H.

Figure 7 plots the surface heat flux, interior temperature, and stagnant lid thickness as a function of the dissipated power, P_{tide}, and for different shell thicknesses. For the two ocean compositions we tested, and independently of the ice shell thickness, both T_m and Φ_{surf} increase with increasing P_{tide}, while the stagnant lid thins. At a given P_{tide}, thicker shells are cooler and transfer less heat, but these changes attenuate as P_{tide} increases. Interestingly, for values of P_{tide} estimated by Hussmann and Spohn (2004), in the range 0.6-1.0 TW, and despite the fact that the bottom heat flux may turn negative (in particular for cases with NH_3 in the ocean), the ice shell may be as thick as 160 km (see also Fig. 6). For slightly larger values, however, D_{melt} sharply decreases with increasing P_{tide}. In the case of a pure water ocean, for instance, it is equal to 120 and 40 km at P_{tide} of 1.1 and 1.3 TW, respectively. Finally, given D_{ice} and P_{tide}, Φ_{surf} decreases with increasing η_{ref}, while T_m increases and the stagnant lid thickens (Figure S5).

5.2 Thermal evolution

We model the ice shell thermal evolution following the approach of Grasset and Sotin (1996), solving the conservation equation of energy at the boundary between this shell and the sub-surface ocean (SI). Again, a detailed reconstruction of this evolution would require to couple Europa's internal and orbital evolutions (Hussmann and Spohn, 2004), implying that the tidal power dissipated within the shell is time-dependent. Instead, we assumed that the dissipated heat does not vary with time.

Examples of evolutions for η_{ref} = 10^{14} Pas are shown in Figure S6. The ice shell first thickens up to a maximum value, and then starts to thin again after a time that depends on input parameters. Note that values of P_{tide} around or larger than 1.5 TW prevents the ocean crystallization. The shell remains thinner than 10 km, and is not animated by convection. Figures 8 and S7 plot the shell properties at time t = 4.55 Gyr as a function of P_{tide} and η_{ref}, respectively. As one could expect, increasing P_{tide} and/or η_{ref} reduces the final shell thickness, D_{ice}, and increases its internal temperature, T_m. In addition, the stagnant lid thickness, d_{lid}, decreases, and convection shuts off at lower η_{ref}. Dissipated powers around or lower than 0.1 TW have no or small impact on D_{ice} and T_m, but still influences d_{lid} substantially. If η_{ref} and/or P_{tide} are too small, the ocean crystallizes completely and remains frozen up to 4.55 Gyr. These conclusions hold for both a pure water ocean and for an ocean with x_{NH3}^{init} = 3.0 vol%. In this later case, however, full crystallization cannot be completed even at low η_{ref} and/or P_{tide}. Furthermore, the effects of impurities are reduced as H increases, such that the shell properties get close to those for a pure water ocean. Internal heating therefore appears as a stronger controlling parameter than the presence of impurities. Finally, it is worth noting that for P_{tide} in the range 0.6-1.0 TW, relevant to Europa (Hussmann et al., 2004), and η_{ref} =10^{14} Pas, Europa's ice shell should be thin, around 20-40 km at a maximum (see also Fig. S6). Lower η_{ref} allows thicker shells, for instance, with η_{ref} = 3.0×10^{13} Pas, up to 120 km (pure water ocean) or 80 km (x_{NH3}^{init} = 3.0 vol%).

6. Conclusions and perspectives

The numerical simulations we performed allowed us to quantify the influence of the rate of internal heating, H, on stagnant-lid convection, through the determination of scaling laws for interior temperature, surface heat flux, and stagnant lid thickness (Table 2). We observed two different regimes depending on the sign of the bottom heat flux, Φ_{bot}, or equivalently, whether the Urey ratio is smaller or larger than 1. Interestingly, our simulations show that the value of H at which Φ_{bot} turns negative increases with increasing thermal viscosity ratio, $\Delta\eta$. Another interesting finding is that, while the stagnant lid stiffens with increasing H, it also thins.

Our simulations include a few simplifications. The rheology of ices is certainly more complex than the Frank-Kamenetskii law we used. Compared to an Arrhenius-type of law, this approach overestimates heat flux by up to 30 % (*e.g.*, Reese et al., 1999). In addition, different mechanisms may control ice Ih deformation depending on the strain rate and/or the grain size, but are not accounted for in our modelling. A full description of ice viscosity may instead require the definition of a composite viscosity law, as proposed by Harel et al. (2020). Our approach further neglects the possible presence of pockets of partially melted ice. Such pockets may occur in plumes heads, right beneath the stagnant lid, in which case they could trigger the formation of chaos and lenticulae regions (Tobie et al., 2003). Melt may also influence the physical properties of ice, in particular its viscosity and density. This would in turn affect the buoyancy of plumes and reduce tidal dissipation, leading to alternate phases of melting and crystallization (Tobie et al., 2003). Vilella et al. (2020) further studied the impact of melt on heat budget, and showed that for internal heating larger than a critical value, heat flux reaches a plateau, as most of the heating is used to generate more melt. While these limitations may quantitatively alter the scaling laws we build, the main trends indicated by our simulations and the conclusions drawn from them should remain unchanged.

A full description of Europa's ice shell evolution requires coupling its orbital and thermal evolutions to capture time-variations in tidal heating. By contrast, calculations coupling Io and Europa evolutions suggest that tidal dissipation within Europa's ice shell may have remained fairly constant around 0.6-1.0 TW during the past 4.5 Gyr (Hussmann and Spohn, 2004). If true, our evolution model should provide first order, but relevant estimates of today Europa's ice shell properties. Taking a reference viscosity in the range 3.0×10^{13}-3.0×10^{14} Pas and assuming the presence of impurities, the thickness of this shell should be in the range 20-75 km. This is larger than estimates from mechanical studies based on surface geology observations (*e.g.*, Billings and Katternhorn, 2005; Damptz and Dombard, 2011; Silber and Johnson, 2017), but consistent with estimates from thermal evolution models (*e.g.*, Tobie et al., 2003; Hussmann and Spohn, 2004; Allu Peddenti and McNamara, 2019; Green et al., 2021) and estimates of the thickness needed to generate melts needed for cryovolcanism (Vilella et al., 2020).

In addition to the evolution of icy bodies, our findings may have some implications for the evolution of planetesimals that formed in early in solar System history. These bodies are thought to have reached a few hundreds of kilometers in size and to have differentiated in a core and a mantle. The decay of ^{26}Al may have released huge amounts of heat in their mantles, which may, in turn, have delayed the cooling of their cores. The scaling laws we obtained can be inserted in thermal evolution models of planetesimals as built, for instance, by Kaminski et al. (2020). Of particular importance is the fact that, all other parameters being the same, Φ_{bot} increases with increasing $\Delta\eta$ and turns negative for values of H that increase with $\Delta\eta$. This suggests that, if stagnant-lid convection, triggered by large top-to-bottom temperature jump, operated within the mantles of planetesimals, large amounts of heat released by the decay of ^{26}Al may have helped, rather than prevented, the cooling of planetesimals cores, and possibly the generation of magnetic fields within these cores.

Acknowledgments

The research presented in this article was supported by the National Science Council of Taiwan (MoST) under grants 108-2116-M-001-017 and 107-2116-M-001-029 (FD), and JSPS KAKENHI Grant JP19F19023 (KV). The data used for generating the figures displayed in this article are available for academic purposes on Academia Sinica institutional repository (Deschamps, 2021b). The code used in this work is not publicly available but was thoroughly described in Tackley (2008).

References

Allu Peddinti, D., & McNamara, A. K. (2019). Dynamical investigation of a thickening ice-shell: Implications for the icy moon Europa. *Icarus*, *329*, 251–269.

Billings, S. E., & Kattenhorn, S. A. (2005). The great thickness debate: Ice shell thickness models for Europa and comparisons with estimates based on flexure at ridges. *Icarus*, *177*, 397–412.

Christensen, U.R. (1984). Heat transport by variable viscosity convection and implications for the Earth's thermal evolution. *Phys. Earth Planet. Inter.*, *35*, 264-282.

Croft, S.K., Lunine, J.I, & Kargel, J. (1988). Equation of state of ammonia-water liquid: .derivation and planetological applications. *Icarus*, *73*, 279-293.

Damptz, A.L., & Dombard, A.J. (2001). Time-dependent flexures of the lithospheres on the icy satellites of Jupiter and Saturn. *Icarus*, *216*, 86-88.

Davaille, A., & Jaupart, C. (1993). Transient high-Rayleigh-number thermal convection with large viscosity variations. *J. Fluid Mech.*, *253*, 141-166.

Deschamps, F. (2021a). Stagnant lid convection with temperature-dependent thermal conductivity and the thermal evolution of icy worlds. *Geophys. J. Int.*, *224*, 1870-1890.

Deschamps, F. (2021b). Scaling laws for mixed-heated stagnant-lid convection and application to Europa. Myspace, Academia Sinica. https://myspace.sinica.edu.tw/public.php?service=files&t=C3tVH2NGcIc1AQSYmc9GAJUCebt5XxUPwhU0Tu1pJeQN8J3cySepAxRwvuUk-W6Q

Deschamps, F., & Sotin, C. (2000). Inversion of two-dimensional numerical convection experiments for a fluid with a strongly temperature-dependent viscosity. *Geophys. J. Int.*, *143*, 204-218.

Deschamps, F., Tackley, P.J., & Nakagawa, T. (2010a). Temperature and heat flux scalings for isoviscous thermal convection in spherical geometry. *Geophys. J. Int.*, *182*, 137-154.

Deschamps, F., Mousis, O., Sanchez-Valle, C. & Lunine, J.I. (2010b). The role of methanol on the crystallization of Titan's primordial ocean. *Astrophys. J.*, *724*, 887-894.

Deschamps, F., & Lin, J.-R. (2014). Stagnant lid convection in 3D-Cartesian geometry: Scaling laws and applications to icy moons and dwarf planets. *Phys. Earth Planet. Inter.*, *229*, 40-54.

Grasset, O. & Sotin, C. (1996). The cooling rate of a liquid shell in Titan's interior. *Icarus*, *123*, 101-112.

Green, A.P., Montesi, L.G.J., & Cooper, C.M. (2021). The growth of Europa's icy shell: convection and crystallization. *J. Geophys. Res. Planets*, *126*, e2020JE006677, doi: 10.1029/2020JE006677.

Guerrero, J., Lowman, J.P., Deschamps, F., & Tackley, P.J. (2018). The influence of curvature on convection in a temperature-dependent viscosity fluid: implications for the 2D and 3D modeling of moons. *J. Geophys. Res. Planets*, *123*, 1863-1880, doi:10.1029/2017JE005497.

Harel, L., Dumoulin, C., Choblet, G., Tobie, G., & Besserer, J. (2020). Scaling of heat transfer in stagnant lid convection for the outer ice shells of icy moons: influence of rheology. *Icarus*, *338*, 113448, doi: 10.106/j.icarus.2019.113448.

Hussmann H. & Spohn, T. (2004). Thermal-orbital evolution of Io and Europa. *Icarus*, *171*, 391-410.

Hussmann, H., Sotin, C. & Lunine, J.I. (2007). Interiors and evolution of icy satellites, in planets and moons, *Treatise on Geophysics*, vol. 10, Elsevier, 509–539.

Kageyama, A., & Sato, T. (2004). "Yin-Yang grid": an overset grid in spherical geometry. *Geochem. Geophys. Geosys.*, *5*, doi: 10.1029/2004GC000734.

Kaminski, E., Limare, A., Kenda, B., & Chaussidon, M. (2020). Early accretion of planetesimals unravelled by the thermal evolution of the parent bodies of magmatic iron meteorites. *Earth Planet. Sci. Lett.*, *548*, 116469, doi: 10.1016/j.epsl.2020.116469.

Khurana, K.K., Kivelson, M.G., Stevenson, D.J., Schubert, G., Russell, C.T., Walker, R.J. & Polanskey, C. (1998). Induced magnetic field as evidence for subsurface ocean in Europa and Callisto. *Nature*, *395*, 777-780.

Montagnat, M. & Duval, P. (2000). Rate controlling processes in the creep of polar ice, influence of grain boundary migration associated with recrystallization. *Earth Planet. Sci. Lett.*, *183*, 179-186.

Moore, W.B. (2008). Heat transport in a convecting layer heated from within and below. *J. geophys. Res.*, *113*, doi:10.1029/2006JB004778.

Moresi, L.-N. & Solomatov, V.S. (1995). Numerical investigation of 2D convection with extremely large viscosity variations. *Phys. Fluids*, **7**, 2154-2162.

Mousis, O., Lunine, J. I., Thomas, C., Pasek, M., Marboeuf, U., Alibert, Y., Ballenegger, V., Cordier, D., Ellinger, Y., Pauzat, F., & Picaud, S. (2009). Clathration of volatiles in the Solar nebula and implications for the origin of Titan's atmosphere. *The Astrophysical Journal*, *691*, 1780-1786.

Roberts, J. H., & Nimmo, F. (2008). Tidal heating and the long-term stability of a subsurface ocean on Enceladus. *Icarus*, *194*, 675–689.

Silber, E. A., & Johnson, B. C. (2017). Impact crater morphology and the structure of Europa's ice shell. *Journal of Geophysical Research Planets*, *122*, 2685–2701.

Stein, C., Lowman, J.P., & Hansen, U. (2013). The influence of mantle internal heating on lithospheric mobility: Implications for super-Earths. *Earth and Planetary Science Letters, 361*, 448–459.

Sotin, C., & Labrosse, S. (1999). Three-dimensional thermal convection in an iso-viscous, infinite Prandtl number fluid heated from within and from below: applications to the transfer of heat through planetary mantles. *Phys. Earth Planet. Inter.*, *112*, 171-190.

Tackley, P.J. (2008). Modelling compressible mantle convection with large viscosity contrasts in a three-dimensional spherical shell using the yin-yang grid. *Phys. Earth Planet. Inter.*, *171*, 7-18.

Tarantola, A. & Valette, B. (1982). Generalized nonlinear inverse problems solved using the least square criterion. *Rev. Geophys. Space Phys.*, *20*, 219-232.

Tobie, G., Choblet, G., & Sotin, C. (2003). Tidally heated convection: constraints on Europa's ice shell thickness. *J. Geophys. Res.*, *108*, doi: 10.1029/2003JE002099.

Tobie, G., Mocquet, A., & Sotin, C. (2005). Tidal dissipation within large icy satellites: Applications to Europa and Titan. *Icarus*, *177*, 534-549.

Travis, B. & Olson, P. (1994). Convection with internal sources and turbulence in the Earth's mantle. *Geophys. J. Int.*, *118*, 1-19.

Vance, S.D., Panning, M.P., Stähler, S. & al., (2018). Geophysical investigations of habitability in ice-covered ocean worlds. *J. Geophys. Res. Planets*, *123*, 180-205.

Vilella, K., & Deschamps, F. (2018). Temperature and heat flux scaling laws for isoviscous infinite Prandtl number mixed heating convection. *Geophys. J. Int.*, *214*, 265-281.

Vilella, K., Choblet, G., Tsao, W.E., & Deschamps, F. (2020). Tidally heated convection and the occurrence of melting in icy satellites: application to Europa. *J. Geophys. Res. Planets*, *125*, e2019JE006248, doi: 10.1029/2019JE006248.

Yao, C., Deschamps, F., Lowman, J.P., Sanchez-Valle, C., & Tackley, P.J. (2014). Stagnant-lid convection in bottom-heated thin 3-D spherical shells: influence of curvature and implications for dwarf planets and icy moons. *J. Geophys. Res. Planets*, *119*, 1895-1913.

Tables

Table 1. Simulations of stagnant-lid convection with mixed heating.

Ra_{surf}	f	$\Delta\eta$	$\widetilde{H}$	$\widetilde{H}_0$	Grid size	$\tilde{T}_m$	$\widetilde{\Phi}_{top}$	$\widetilde{\Phi}_{bot}$	Ur	$rms(\tilde{v})$	$\tilde{v}_{surf}$	Ra_{eff}	$\tilde{d}_{lid}$	$\tilde{T}_{lid}$
							3D-Cartesian							
16.0	-	10^4	4.0		128×128×64	1.075	3.458	-0.543	1.16	26.9	1.2×10^{-1}	3.19×10^5	0.316	0.892
32.0	-	10^4	2.0		128×128×64	0.969	2.836	0.837	0.71	40.6	3.8×10^{-1}	2.40×10^5	0.324	0.814
32.0	-	10^4	3.0		128×128×64	1.016	3.222	0.223	0.93	39.9	2.9×10^{-1}	3.71×10^5	0.302	0.835
32.0	-	10^4	4.0		128×128×64	1.051	3.678	-0.323	1.09	41.3	2.2×10^{-1}	5.12×10^5	0.280	0.872
75.0	-	10^4	1.5		128×128×64	0.937	3.202	1.702	0.47	76.9	1.01	4.21×10^5	0.268	0.804
75.0	-	10^4	3.0		128×128×64	0.998	3.668	0.670	0.82	69.7	5.4×10^{-1}	7.36×10^5	0.249	0.820
75.0	-	10^4	5.0		256×256×128	1.059	4.577	-0.422	1.09	73.4	2.5×10^{-1}	1.05×10^6	0.221	0.889
17.9	-	3.2×10^4	2.0		128×128×64	0.977	2.887	0.887	0.69	52.1	1.3×10^{-1}	4.51×10^5	0.323	0.828
17.9	-	3.2×10^4	4.0		128×128×64	1.042	3.740	-0.260	1.07	53.5	8.2×10^{-2}	8.85×10^5	0.276	0.880
55.9	-	3.2×10^4	0.0		128×128×64	0.874	3.000	3.001	0.00	112.5	7.1×10^{-1}	4.84×10^5	0.254	0.762
55.9	-	3.2×10^4	1.0		128×128×64	0.922	3.374	2.376	0.30	120.7	5.6×10^{-1}	7.92×10^5	0.252	0.818
55.9	-	3.2×10^4	2.0		256×256×128	0.962	3.649	1.649	0.55	117.4	2.6×10^{-1}	1.21×10^6	0.249	0.847
55.9	-	3.2×10^4	3.0		256×256×128	0.990	3.959	0.959	0.76	104.8	2.0×10^{-1}	1.62×10^6	0.233	0.840
55.9	-	3.2×10^4	6.0		256×256×128	1.069	5.352	-0.648	1.12	116.2	1.3×10^{-2}	3.65×10^6	0.192	0.917
178.9	-	3.2×10^4	4.0		256×256×128	0.985	5.344	1.343	0.75	198.9	5.4×10^{-1}	4.92×10^6	0.168	0.843
10.0	-	10^5	2.0		128×128×64	0.975	2.976	0.977	0.67	69.7	5.7×10^{-1}	7.62×10^5	0.319	0.849
10.0	-	10^5	4.0		256×256×128	1.034	3.818	-0.181	1.05	69.1	4.1×10^{-2}	1.38×10^6	0.273	0.894
10.0	-	10^5	6.0		256×256×128	1.110	5.007	-0.994	1.20	96.4	2.4×10^{-1}	3.60×10^6	0.224	0.971
31.6	-	10^5	0.0		256×256×128	0.891	3.143	3.144	0.00	148.1	3.0×10^{-1}	9.06×10^5	0.257	0.809
31.6	-	10^5	0.492	1.0	256×256×128	0.915	3.276	2.785	0.15	156.4	2.4×10^{-1}	1.18×10^6	0.257	0.842
31.6	-	10^5	2.0		256×256×128	0.964	3.772	1.774	0.53	148.2	1.2×10^{-1}	2.08×10^6	0.244	0.860
31.6	-	10^5	2.096	3.0	256×256×128	0.982	3.493	1.397	0.60	132.2	7.2×10^{-2}	2.57×10^6	0.246	0.858
31.6	-	10^5	4.0		256×256×128	1.006	4.471	0.471	0.89	132.6	7.3×10^{-2}	3.38×10^6	0.214	0.866
31.6	-	10^5	5.0		256×256×128	1.028	4.898	-0.101	1.02	133.7	7.2×10^{-2}	4.35×10^6	0.202	0.889
31.6	-	10^5	6.0		256×256×128	1.054	5.447	-0.553	1.10	145.7	6.6×10^{-2}	5.88×10^6	0.187	0.915
50.6	-	10^5	2.0		256×256×128	0.957	4.236	2.236	0.47	195.8	1.5×10^{-1}	3.08×10^6	0.214	0.861
50.6	-	10^5	3.0		256×256×128	0.979	4.501	1.502	0.67	169.1	1.3×10^{-1}	3.97×10^6	0.201	0.843
50.6	-	10^5	3.022	4.0	256×256×128	0.991	4.182	1.159	0.72	170.4	8.9×10^{-2}	4.58×10^6	0.206	0.860
50.6	-	10^5	6.0		256×256×128	1.035	5.710	-0.290	1.05	179.8	1.1×10^{-1}	7.60×10^6	0.174	0.900

Table 1 *(continued)*.

Ra_{surf}	f	$\Delta\eta$	$\tilde{H}$	$\tilde{H}_0$	Grid size	$\tilde{T}_m$	$\tilde{\Phi}_{top}$	$\tilde{\Phi}_{bot}$	Ur	$rms(\tilde{v})$	$\tilde{v}_{surf}$	Ra_{eff}	$\tilde{d}_{lid}$	$\tilde{T}_{lid}$
50.6	-	10^5	8.0		256×256×128	1.089	6.970	-1.029	1.15	226.5	7.9×10^{-2}	1.41×10^7	0.149	0.952
50.6	-	10^5	10.0		256×256×128	1.145	8.427	-1.573	1.19	313.9	6.7×10^{-2}	2.70×10^7	0.129	1.007
56.6	-	3.2×10^5	4.0		256×256×128	0.980	5.685	1.685	0.70	326.6	9.4×10^{-2}	1.41×10^7	0.161	0.864
56.6	-	3.2×10^5	8.0		256×256×128	1.040	7.461	-0.539	1.07	354.8	7.4×10^{-2}	2.99×10^7	0.132	0.914
113.1	-	3.2×10^5	4.0		256×256×128	0.970	6.600	2.602	0.61	486.3	2.3×10^{-1}	2.48×10^7	0.137	0.867
10.0	-	10^6	1.0		256×256×128	0.940	3.913	2.914	0.31	266.4	4.0×10^{-2}	4.38×10^6	0.232	0.880
10.0	-	10^6	2.0		256×256×128	0.963	4.162	2.164	0.48	240.1	2.7×10^{-2}	5.97×10^6	0.227	0.894
10.0	-	10^6	3.0		256×256×128	0.981	4.455	1.456	0.67	213.7	2.1×10^{-2}	7.74×10^6	0.209	0.865
10.0	-	10^6	4.0		256×256×128	0.995	4.755	0.754	0.84	216.69	1.5×10^{-2}	9.33×10^6	0.203	0.882
10.0	-	10^6	4.251	5.5	256×256×128	1.012	4.442	0.192	0.96	216.81	1.7×10^{-2}	1.18×10^7	0.205	0.912
10.0	-	10^6	5.0		256×256×128	1.010	5.179	0.178	0.97	217.0	1.8×10^{-1}	1.15×10^7	0.190	0.895
10.0	-	10^6	6.0		256×256×128	1.030	5.689	-0.312	1.05	227.3	1.5×10^{-1}	1.51×10^7	0.177	0.915
10.0	-	10^6	8.0		256×256×128	1.082	7.007	-0.994	1.14	308.3	1.4×10^{-1}	3.11×10^7	0.150	0.963
25.0	-	10^6	0.0		256×256×128	0.912	4.415	4.416	0.00	456.1	2.8×10^{-1}	7.38×10^6	0.193	0.850
25.0	-	10^6	2.0		256×256×128	0.952	5.234	3.235	0.38	371.5	3.8×10^{-2}	1.29×10^7	0.171	0.868
25.0	-	10^6	2.059	3.0	256×256×128	0.959	4.984	2.926	0.41	370.8	4.5×10^{-2}	1.42×10^7	0.179	0.892
25.0	-	10^6	3.0		256×256×128	0.969	5.426	2.428	0.55	367.6	2.2×10^{-2}	1.63×10^7	0.169	0.873
25.0	-	10^6	3.041	4.0	256×256×128	0.977	5.059	2.016	0.60	355.2	3.3×10^{-2}	1.82×10^7	0.176	0.892
25.0	-	10^6	4.0		256×256×128	0.981	5.639	1.637	0.71	361.3	4.3×10^{-2}	1.92×10^7	0.165	0.876
25.0	-	10^6	4.929	6.0	256×256×128	1.001	5.564	0.635	0.89	361.2	4.6×10^{-2}	2.54×10^7	0.163	0.905
25.0	-	10^6	6.0		256×256×128	1.006	6.392	0.394	0.94	366.8	3.6×10^{-2}	2.71×10^7	0.150	0.889
25.0	-	10^6	8.0		256×256×128	1.037	7.450	-0.550	1.07	403.1	3.3×10^{-2}	4.14×10^7	0.133	0.922
45.0	-	10^6	4.0		256×256×128	0.973	6.377	2.380	0.63	515.9	8.5×10^{-2}	3.10×10^7	0.144	0.875
5.6	-	3.2×10^6	4.0		256×256×128	0.992	4.957	0.956	0.81	281.6	1.1×10^{-1}	1.57×10^7	0.194	0.886
5.6	-	3.2×10^6	8.0		256×256×128	1.065	7.130	-0.870	1.12	377.2	7.4×10^{-2}	4.71×10^7	0.146	0.958
41.9	-	3.2×10^6	4.0		256×256×128	0.967	7.495	3.496	0.53	937.6	5.4×10^{-2}	8.18×10^7	0.123	0.892
10.0	-	10^7	0.0		256×256×128	0.923	5.271	5.278	0.00	964.4	8.9×10^{-2}	2.94×10^7	0.165	0.869
10.0	-	10^7	2.948	4.0	256×256×128	0.969	6.089	3.142	0.48	753.1	1.9×10^{-2}	6.14×10^7	0.152	0.926
10.0	-	10^7	4.0		256×256×128	0.975	6.568	2.571	0.61	732.8	1.5×10^{-2}	6.76×10^7	0.149	0.935
10.0	-	10^7	8.0		384×384×192	0.940	8.115	0.114	0.99	734.9	1.1×10^{-2}	1.15×10^8	0.121	0.920
10.0	-	10^7	10.0		384×384×192	1.035	9.325	-0.676	1.07	851.5	1.0×10^{-2}	1.79×10^8	0.108	0.948
3.2	-	10^8	0.0		384×384×192	0.934	6.000	5.999	0.00	1228.2	2.0×10^{-2}	9.46×10^7	0.147	0.885
3.2	-	10^8	2.871	4.0	384×384×192	0.967	6.857	3.986	0.42	1353.7	4.8×10^{-3}	1.74×10^8	0.137	0.941
3.2	-	10^8	4.0		384×384×192	0.971	7.403	3.401	0.54	1328.9	4.0×10^{-3}	1.88×10^8	0.127	0.909

Table 1 *(continued)*.

Ra_{surf}	f	$\Delta\eta$	$\widetilde{H}$	$\widetilde{H}_0$	Grid size	$\tilde{T}_m$	$\widetilde{\Phi}_{top}$	$\widetilde{\Phi}_{bot}$	Ur	$rms(\tilde{v})$	$\tilde{v}_{surf}$	Ra_{eff}	$\tilde{d}_{lid}$	$\tilde{T}_{lid}$
							Spherical							
16.0	0.60	10^6	4.0		192×576×96×2	0.932	3.970	3.767	0.67	242.7	8.0×10^{-2}	6.25×10^6	0.221	0.859
16.0	0.60	10^6	10.0		192×576×128×2	1.034	6.313	-0.607	1.03	307.6	2.2×10^{-2}	2.55×10^7	0.155	0.918
5.1	0.60	10^7	4.0		192×576×128×2	0.929	4.389	4.928	0.60	396.0	2.1×10^{-2}	1.64×10^7	0.204	0.887
10.0	0.70	10^6	8.0		192×576×96×2	0.964	3.964	2.129	0.74	193.4	3.5×10^{-2}	6.12×10^6	0.228	0.861
10.0	0.70	10^6	8.0		256×768×128×2	1.035	5.596	-0.498	1.04	234.5	1.7×10^{-2}	1.61×10^7	0.177	0.918
3.2	0.70	10^7	8.0		256×768×128×2	1.011	5.833	-0.011	1.00	366.1	4.4×10^{-2}	3.78×10^7	0.167	0.908
10.0	0.70	10^7	2.0		192×576×128×2	0.907	4.914	7.046	0.30	622.9	6.1×10^{-2}	2.23×10^7	0.171	0.854
15.8	0.70	10^7	3.0		192×576×128×2	0.917	5.845	7.461	0.37	797.0	5.8×10^{-2}	4.15×10^7	0.149	0.879
3.2	0.75	10^7	4.0		256×768×128×2	0.964	4.530	2.568	0.68	346.0	9.2×10^{-2}	1.78×10^7	0.206	0.894
3.2	0.75	10^7	8.0		256×768×128×2	1.017	6.049	-0.208	1.02	378.8	4.2×10^{-2}	4.19×10^7	0.162	0.915
3.2	0.75	10^7	10.0		256×768×128×2	1.054	7.188	-0.923	1.07	496.3	3.5×10^{-2}	7.49×10^7	0.141	0.950
10.0	0.75	10^7	4.0		256×768×128×2	0.945	5.834	4.883	0.53	660.7	2.0×10^{-2}	4.19×10^7	0.155	0.892
10.0	0.75	10^7	10.0		384×1152×192×2	1.005	7.817	0.192	0.99	716.3	9.1×10^{-3}	1.10×10^8	0.123	0.912
10.0	0.80	10^6	2.0		256×768×96×2	0.938	3.617	3.107	0.45	223.4	7.4×10^{-2}	4.25×10^6	0.242	0.859
10.0	0.80	10^6	4.0		256×768×96×2	0.977	4.267	1.580	0.76	192.0	3.0×10^{-2}	7.18×10^6	0.213	0.857
10.0	0.80	10^6	8.0		256×768×128×2	1.051	6.039	-0.729	1.08	258.1	1.6×10^{-2}	2.02×10^7	0.168	0.931
10.0	0.80	10^6	10.0		256×768×128×2	1.098	7.289	-1.315	1.12	366.4	1.3×10^{-2}	3.89×10^7	0.144	0.978
32.0	0.80	10^6	4.0		256×768×128×2	0.952	5.412	3.368	0.60	404.7	1.7×10^{-1}	1.65×10^7	0.167	0.879
3.2	0.80	10^7	4.0		256×768×128×2	0.972	4.666	2.205	0.70	359.2	1.1×10^{-2}	2.02×10^7	0.201	0.893
3.2	0.80	10^7	8.0		256×768×128×2	1.025	6.253	-0.395	1.04	401.8	3.8×10^{-3}	4.69×10^7	0.159	0.922
3.2	0.80	10^7	10.0		256×768×128×2	1.058	7.503	-0.979	1.08	557.2	4.6×10^{-3}	7.99×10^7	0.134	0.951
1.0	0.80	10^8	4.0		512×1536×192×2	0.966	5.266	3.157	0.62	626.5	2.5×10^{-3}	5.32×10^7	0.181	0.920
3.2	0.80	10^8	3.0		512×1536×192×2	0.940	6.482	6.387	0.38	1250.1	1.1×10^{-2}	1.11×10^8	0.144	0.930
10.0	0.85	10^6	4.0		256×768×128×2	0.983	4.403	1.345	0.78	201.5	2.6×10^{-2}	7.86×10^6	0.215	0.883
10.0	0.85	10^6	8.0		256×768×128×2	1.058	6.253	-0.838	1.10	283.1	1.4×10^{-2}	2.23×10^7	0.164	0.940

Listed parameters are the surface Rayleigh number, Ra_{surf}, the inner-to-outer radii ratio (for spherical cases), f, the top-to-bottom thermal viscosity ratio, $\Delta\eta$, the non-dimensional rate of internal heating, $\widetilde{H}$, the constant $\widetilde{H}_0$ (for heterogeneous internal heating cases, Eq. 9), the grid size, the average non-dimensional temperature of the well-mixed interior, $\tilde{T}_m$, the top and bottom non-dimensional heat fluxes, $\widetilde{\Phi}_{top}$ and $\widetilde{\Phi}_{bot}$, the Urey ratio, Ur (Eq. 12), the root mean square velocity of the whole system, $rms(\tilde{v})$, the average surface velocity, $\tilde{v}_{surf}$, the effective Rayleigh number, Ra_{eff} (Eq. 10), the non-dimensional thickness of the stagnant lid, $\tilde{d}_{lid}$, calculated following the method of Davaille and Jaupart (1993), and the temperature at the base of this lid, $\tilde{T}_{lid}$, deduced from Eq. (19) or Eq. (20) with observed values of $\widetilde{\Phi}_{top}$ and $\tilde{d}_{lid}$. Calculations with pure bottom heating ($\widetilde{H} = 0$) are taken from Deschamps and Lin (2014).

Table 2. Summary of scaling laws

Quantity	Expression	Parameters		
		Symbol	*Ur* < 1	*Ur* > 1
Interior temperature	$\tilde{T}_m = 1 - a_1/f^{a_2}\gamma + (c_1 + c_2 f)\left[\tilde{H}(1 + f + f^2)/3\right]^{c_4}/{Ra_{eff}}^{c_3}$	a_1	1.23	1.23
		a_2	1.5	1.5
		c_1	3.5	4.4
		c_2	-2.3	-3.0
		c_3	0.25	1/3
		c_4	1.0	1.72
Surface heat flux	$\tilde{\Phi}_{top} = a\, {Ra_{eff}}^{b}/\gamma^c$	a	1.46	1.57
		b	0.27	0.27
		c	1.21	1.21
Stagnant lid thickness	$\tilde{d}_{lid} = a_{lid}\, \gamma^c/{Ra_{eff}}^{b}$	a_{lid}	0.633	0.667
		b	0.27	0.27
		c	1.21	1.21
Threshold internal heating	$\tilde{H}_{crit} = 3a_H \exp(c_H\gamma) Ra_{surf}^{b_H}/(1 + f + f^2)$	a_H	0.184	
		b_H	0.31	
		c_H	0.19	

Listed expressions are scaling laws for non-dimensional interior temperature, $\tilde{T}_m$, surface heat flux, $\tilde{\Phi}_{top}$, stagnant lid thickness, $\tilde{d}_{lid}$, and internal heating at the transition between positive (*Ur* < 1) and negative (*Ur* > 1) bottom heat flux, $\tilde{H}_{crit}$. In these expressions, $\tilde{H}$ is the internal heating, f the ratio between inner and outer radii (equal to 1 for Cartesian geometry), Ra_{surf} the surface Rayleigh number, and Ra_{eff} the effective Rayleigh number calculated at $\tilde{T} = \tilde{T}_m$, given by Eq. (10). The parameter γ, controlling the amplitude of viscosity changes with temperature, is given by $\gamma = \Delta T/\Delta T_v$, where ΔT_v is the viscous temperature scale (Eq. 22). Parameter values are inferred by best fitting these expressions to the results of numerical simulations listed in Table 1.

Table 3. Europa and materials properties

Parameter	Symbol	Unit	Value/Expression	Europa
Ice Ih properties				
Density	ρ_I	kg/m^3	920	
Thermal expansion	α_I	1/K	1.56×10^{-4}	
Thermal conductivity	k_I	W/m/K	$566.8/T$	
Heat capacity	C_p	J/kg/K	$7.037T + 185$	
Thermal diffusivity	κ_I	m^2/s	$k/\rho_I C_p$	
Latent heat of fusion	L_I	kJ/kg	284	
Reference bulk viscosity	η_{ref}	Pa s	10^{12}-10^{15}	
Activation energy	E	kJ/mol	60	
Liquid water/ammonia properties				
Density (water)	ρ_w	kg/m^3	1000	
Density (ammonia)	ρ_{NH3}	kg/m^3	734	
Thermal expansion (water)	α_w	1/K	3.0×10^{-4}	
Heat capacity (water)	C_w	J/kg/K	4180	
Silicate core properties				
Density	ρ_c	kg/m^3	3300	
Thermal diffusivity	κ_c	m^2/s	10^{-6}	
Europa properties				
Total radius	R	km		1561
Core radius	r_c	km		1400
Gravity acceleration	g	m/s^2		1.31
Surface temperature	T_{surf}	K		100
Surface thermal conductivity	k_{surf}	W/m/K		5.7

All data for ice Ih and liquid water properties are similar to that used by Kirk and Stevenson (1987) (see references therein), except liquid ammonia density, which is from Croft et al. (1988), bulk viscosity, which is a free parameter with possible range of values extended from Montagnat and Duval (2000) estimates, and the activation energy, which is taken from the intermediate regime of Durham et al. (2010).

Figures

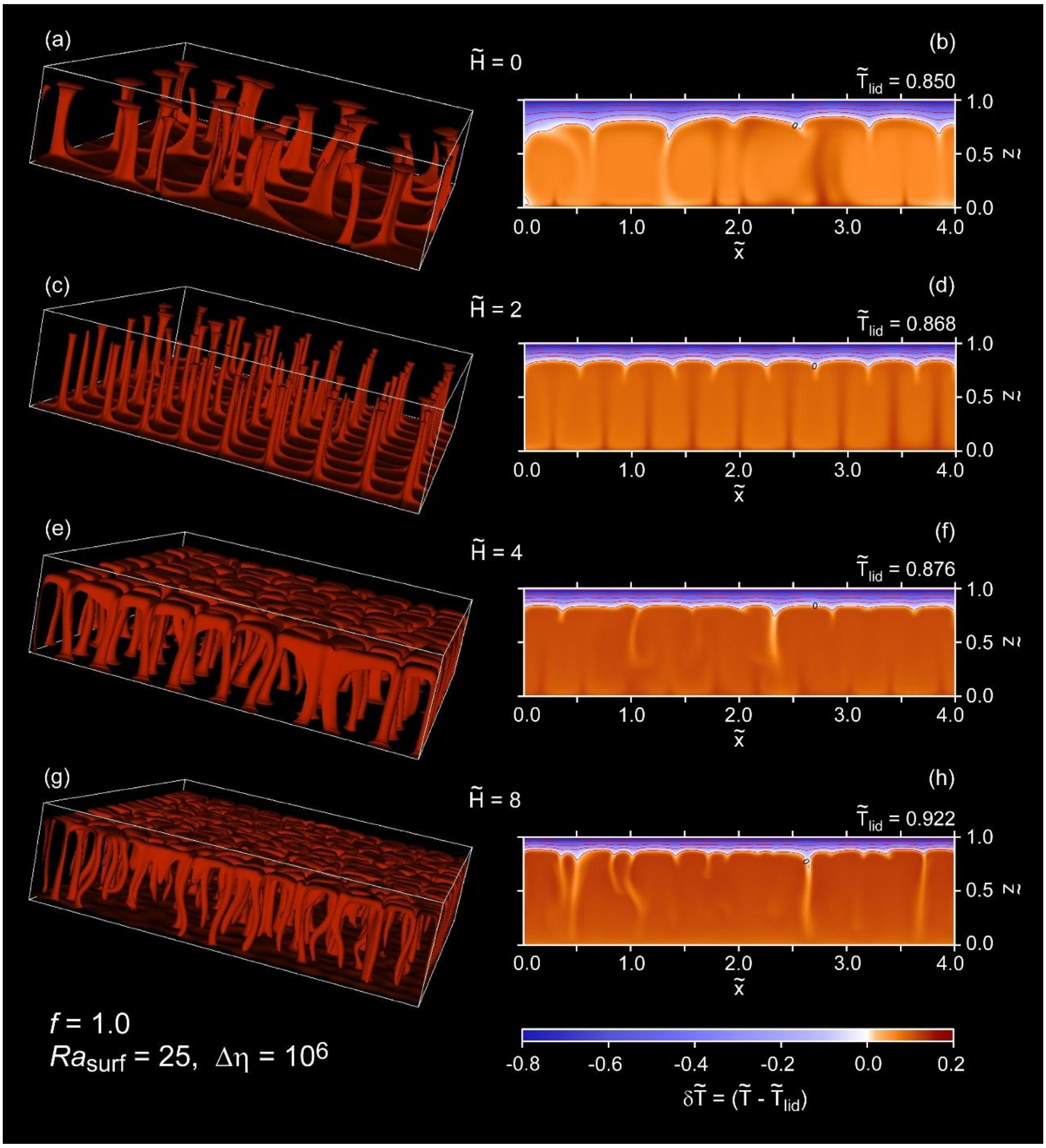

Figure 1. Snapshots of the temperature field (left) and vertical slices of the residual temperature relative to the temperature at the bottom of the stagnant lid $\tilde{T}_{lid}$ (right) for cases with surface Rayleigh number $Ra_{\mathrm{surf}} = 25$, thermal viscosity ratio $\Delta\eta = 10^6$ and different values of the non-dimensional rate of internal heating, $\tilde{H}$. (a-b) $\tilde{H} = 0$ (pure bottom heating), (c-d) $\tilde{H} = 2$, (e-f) $\tilde{H} = 4$, and (g-h) $\tilde{H} = 8$. Isosurface values are (a) $\tilde{T} = 0.95$, (c) $\tilde{T} = 0.97$, (e) $\tilde{T} = 0.95$, and (g) $\tilde{T} = 1.015$. In the case with $\tilde{H} = 8$ (plots g-h) the bottom heat flux is negative, *i.e.*, the system cools down both at its top and its bottom. Value of $\tilde{T}_{lid}$ are indicated on each panel.

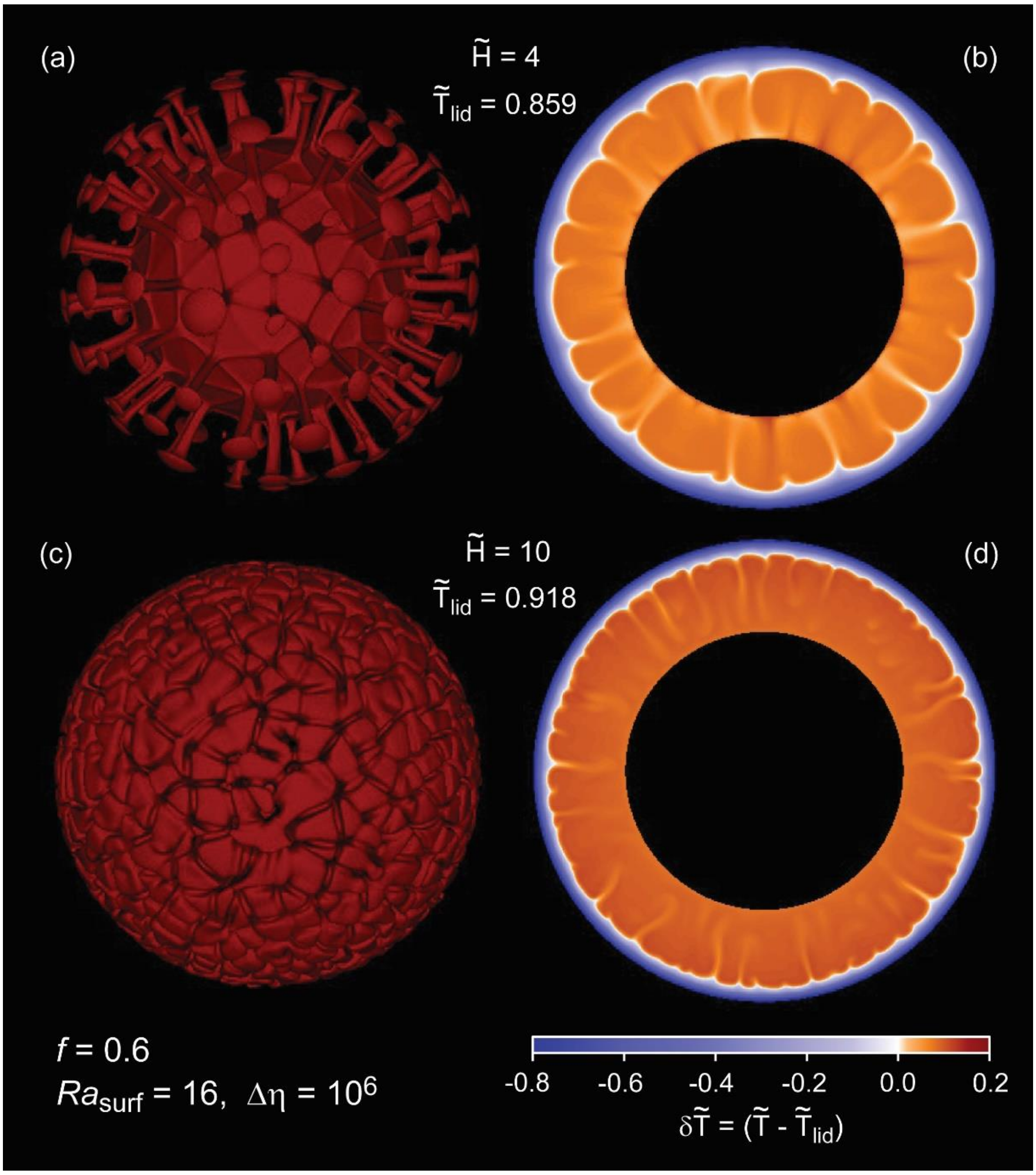

Figure 2. Isosurface of the temperature (left) and polar slices of the residual temperature relative to the temperature at the bottom of the stagnant lid $\tilde{T}_{lid}$ (right) for snapshots of two cases in 3D-spherical geometry with f = 0.6, surface Rayleigh number Ra_{surf} = 16, thermal viscosity ratio $\Delta\eta = 10^6$ and two values of the non-dimensional rate of internal heating, $\tilde{H} = 4$, (a-b) and $\tilde{H} = 10$ (c-d). Isosurface values are $\tilde{T} = 0.95$ in plot (a) and $\tilde{T} = 1.03$ in plot (c). In the case with $\tilde{H} = 10$ (plots c-d), the bottom heat flux is negative, *i.e.*, the system cools down both at its top and its bottom. Value of $\tilde{T}_{lid}$ are indicated on each panel.

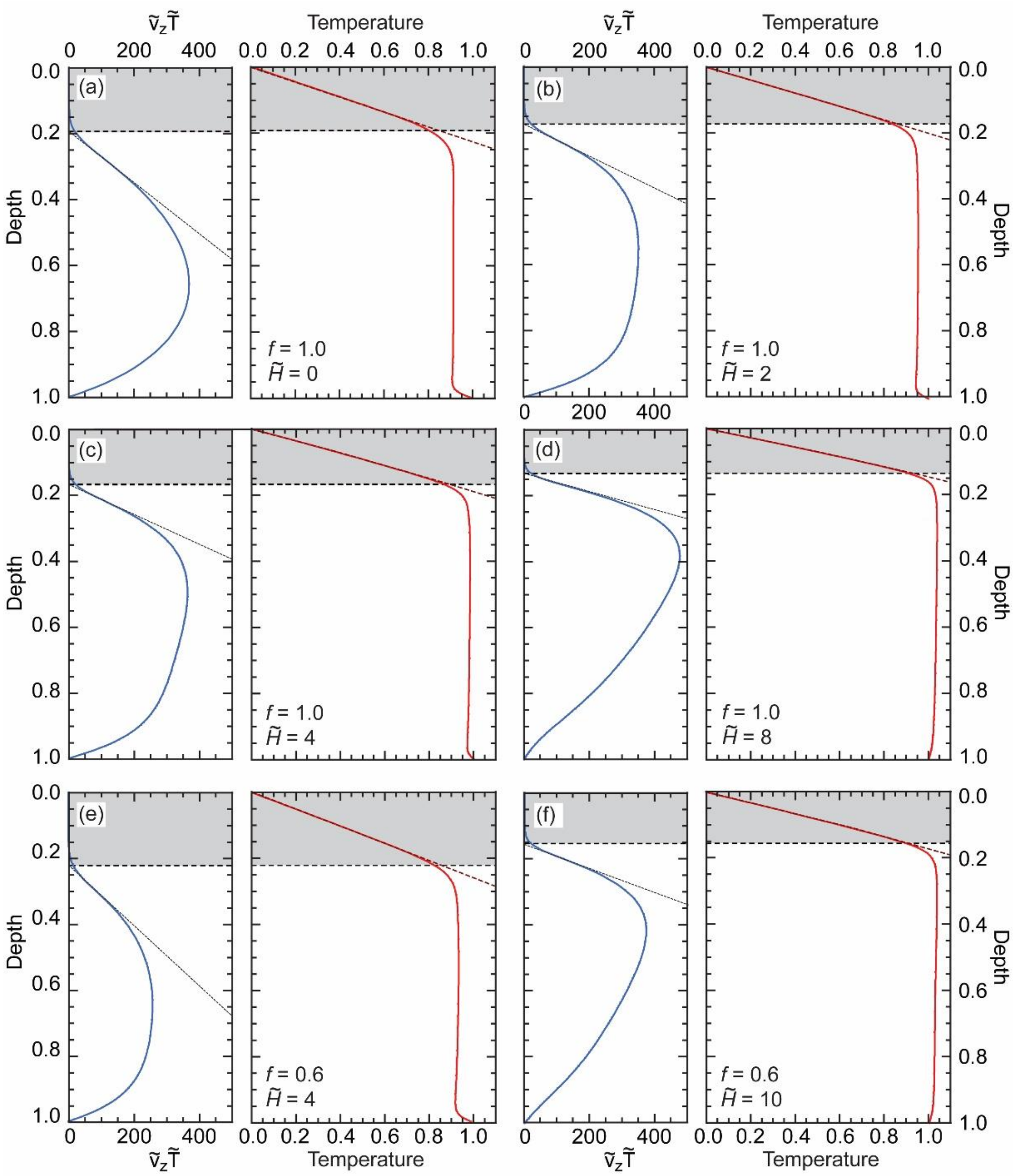

Figure 3. Horizontally averaged profiles of temperature (right plot in each panel) and vertically advected heat flow (left plot) for four cases in 3D-Cartesian geometry (plots a-d) and two cases in 3D-spherical geometry with inner-to-outer radii ratio f = 0.6 (plots e-f). Surface Rayleigh number, Ra_{surf}, is equal to 25 for 3D-Cartesian cases and 16 for spherical cases, and the top-to-bottom viscosity ratio is $\Delta\eta = 10^6$ in all cases. The non-dimensional heating rate is (a) $\tilde{H} = 0$, (b) $\tilde{H} = 2$, (c) $\tilde{H} = 4$, (d) $\tilde{H} = 8$, (e) $\tilde{H} = 4$, (f) $\tilde{H} = 10$. The grey areas denote the vertical extension of the stagnant lid. The dashed lines in the plots of advected heat flow show the tangent to the point of inflexion, whose intersection with the origin axis defines the bottom of the lid. The dashed dark-red curves in the plots of temperature are determined assuming a conductive temperature profile in the stagnant lid, and are calculated following either $\tilde{T}(\tilde{z}) = \tilde{T}_{lid}\, z/\tilde{d}_{lid}$ (panel a), Eq. (15) (panels b-d) or Eq. (16) (panel e-f) with values of $\tilde{d}_{lid}$ listed in Table 1, and values of $\tilde{T}_{lid}$ estimated from Eq. (19) or Eq. (20).

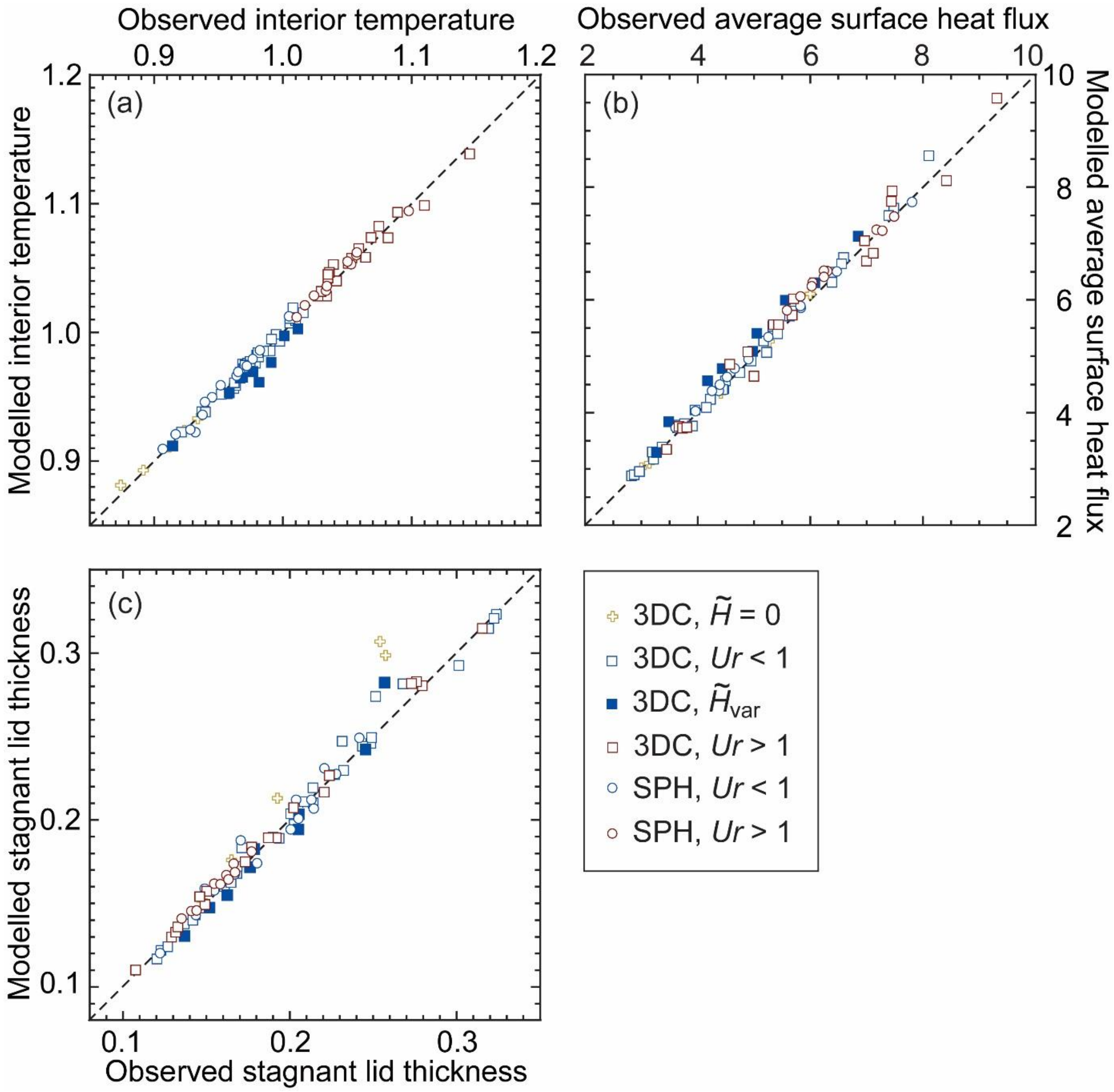

Figure 4. Comparison between observed and modelled output properties. (a) Temperature of the well-mixed interior, $\tilde{T}_m$. Observed values are listed in Table 1, and modelled values are given by Eq. (21) with parameter values discussed in section 4.1. (b) Surface heat flux, $\tilde{\Phi}_{top}$. Observed values are listed in Table 1, and modelled values are calculated by Eq. (23) with parameter values discussed in section 4.2. (c) Thickness of the stagnant lid, $\tilde{d}_{lid}$. Observed values are listed in Table 1, and modelled values are calculated by Eq. (26) with parameter values discussed in section 4.4.

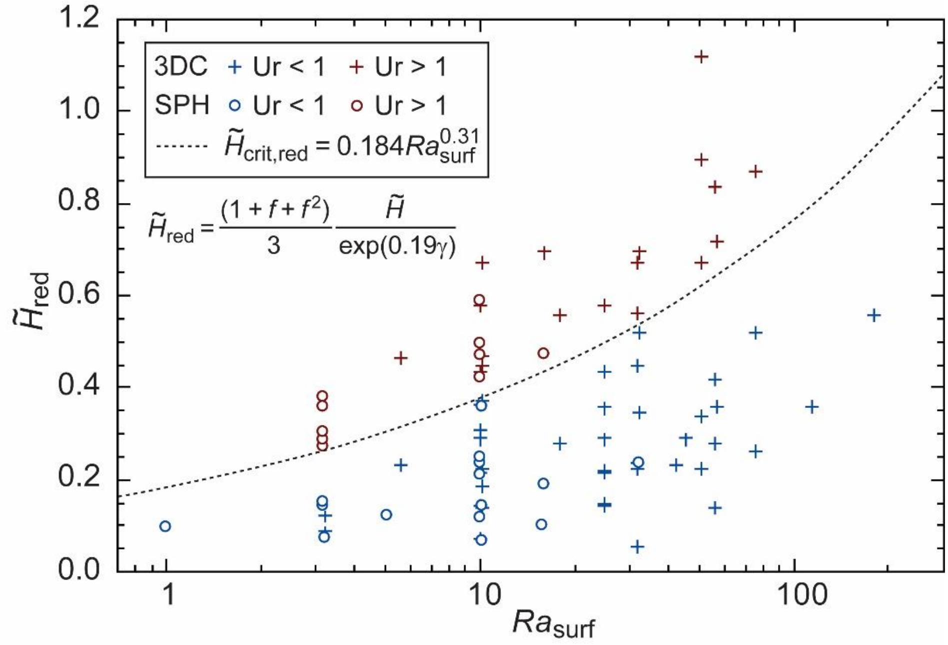

Figure 5. Reduced non-dimensional heating rate, $\widetilde{H}_{red} = \exp(0.19\gamma)\,(1 + f + f^2)/3$, as a function of surface Rayleigh number, Ra_{surf}. Blue and red symbols plot our numerical simulations (Table 1) with positive and negative bottom heat flux, respectively, and the dashed curve shows the (reduced) critical rate of internal heating for which the bottom heat flux turns negative, $\widetilde{H}_{crit}$, calculated with Eq. (25).

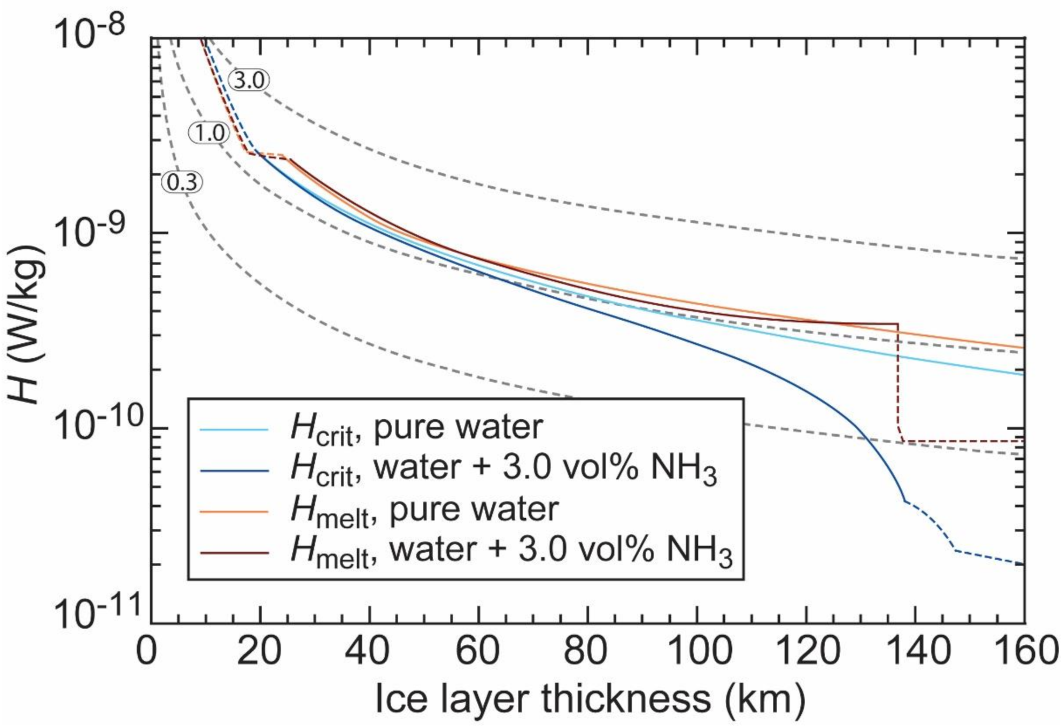

Figure 6. Critical values of internal heating for the transition between a positive and negative bottom heat flux, H_{crit}, and for partial melting of the ice shell, H_{melt}, as a function of the ice shell thickness. Calculations are made with the properties of Europa (Table 3), $\eta_{\text{ref}} = 10^{14}$ Pa s, and for two possible compositions of the sub-surface ocean, pure water and an initial mix (*i.e.*, for a shell thickness equal to 0) of water and 3.0 vol% ammonia. Dashed parts of the curves indicate that the system is not animated by convection, based on the observation that the convective heat flux is smaller than the corresponding conductive heat flux. The grey dashed curves represent the heating rate for three values of the total power dissipated within the ice shell (values in TW indicated on each curve).

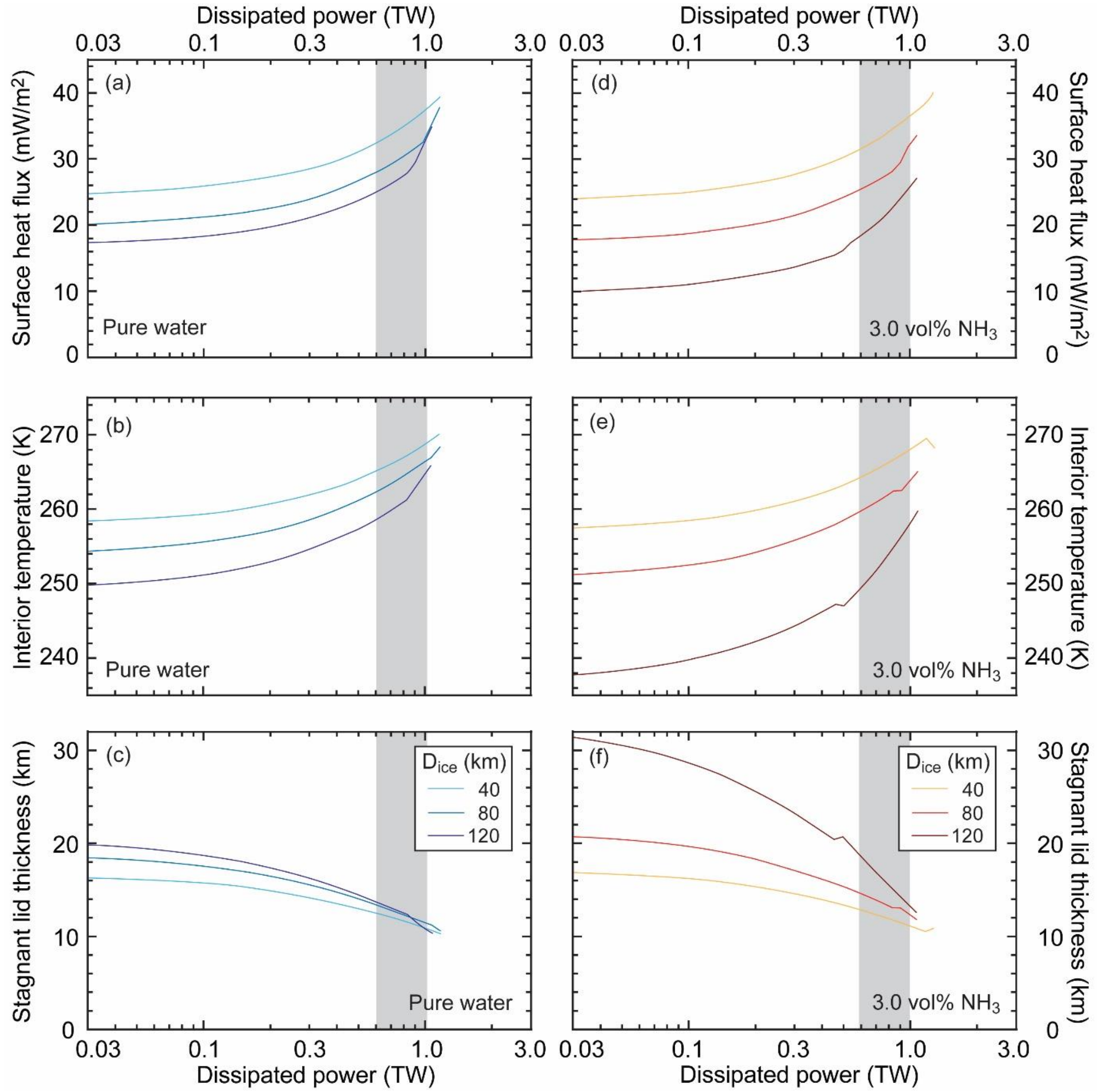

Figure 7. Properties of Europa's outer ice shell as a function of the power dissipated within this shell, and for three selected shell thicknesses (color code). (a) and (d) Surface heat flux. (b) and (e) Interior temperature. (c) and (f) Stagnant lid thickness. Physical properties used for calculations are listed in Table 3, the reference viscosity η_{ref} is equal to 10^{14} Pa s, and two initial compositions of the ocean are considered, pure water (left column), and an initial mix of water and 3.0 vol% ammonia (right column). Curves interruptions indicate that the average interior temperature is larger than the liquidus of pure water at this depth. For the cases with ammonia, two regimes occur depending on whether the Urey ratio (*Ur*, Eq. 12) is smaller or larger than 1, leading to discontinuities at *Ur* ~ 1. The grey shaded bands represent the possible range of dissipated power according to Hussman and Spohn (2004).

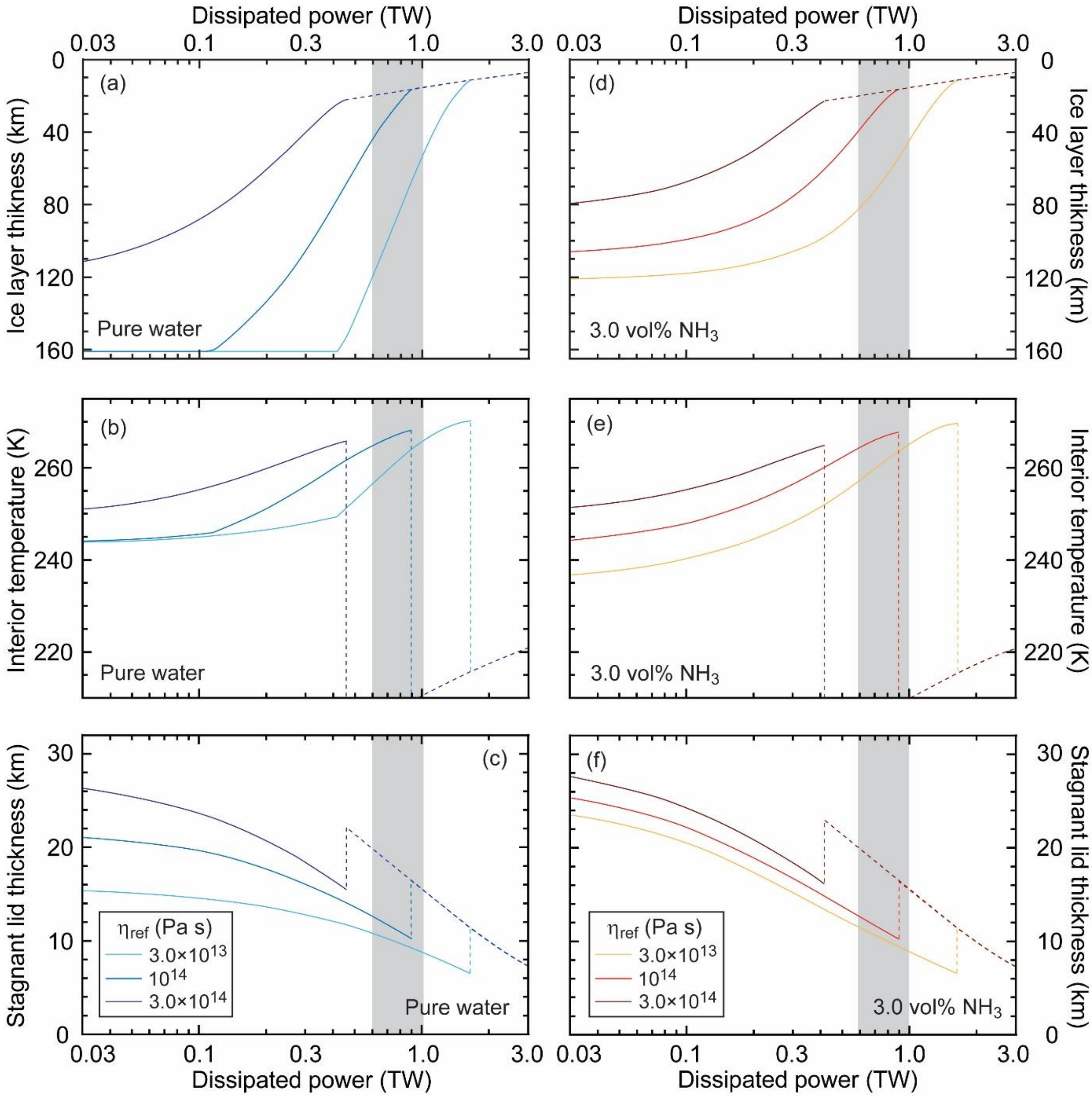

Figure 8. Properties of Europa's outer ice shell at t = 4.55 Gyr as a function of the power dissipated within the shell and for three values of the reference viscosity, η_{ref} (color code). (a) and (d) Thickness. (b) and (e) Interior temperature. (c) and (f) Stagnant lid thickness. Physical properties used for calculations are listed in Table 3, and two initial compositions of the ocean are considered, pure water (left column), and an initial mix of water and 3.0 vol% ammonia (right column). Dashed parts of the curves indicate that the system is not animated by convection. The grey shaded bands represent the possible range of dissipated power according to Hussman and Spohn (2004).

Supporting information for "Scaling laws for mixed-heated stagnant lid convection and application to Europa"

Frédéric Deschamps[1] and Kenny Vilella[2]

[1] Institute of Earth Sciences, Academia Sinica, 128 Academia Road Sec. 2, Nangang, Taipei 11529, Taiwan. [2] JSPS International Research Fellow, Hokkaido University, Sapporo, Japan.

This supporting information provides details on the calculation of radial conductive profiles of temperature and heat flux for a mixed-heated system (section S1 and Table S1), and on the trends predicted by scaling laws for interior temperature and surface heat flux (section S2 and Figures S1 and S2). It further describes the methods used to calculate the ice shell properties (heat flux, interior temperature, and stagnant lid thickness ; section S3 and Figures S3 to S5) and the thermal evolution of this shell (section S4 and Figures S6 and S7). Our modelling is mostly similar to that used in Deschamps (2021). Major differences are the treatments of the interior temperature and stagnant lid thickness.

S1. Temperature and heat flux profiles for stagnant lids in mixed-heated systems

S1.1 Temperature and heat flux profiles in conductive mixed-heated systems

Radial profiles of temperature and heat flux for a purely conductive system with internal heat production may be obtained by integrating the heat equation, which writes

$$\frac{\partial}{\partial z}\left(k\frac{\partial T}{\partial z}\right) + \bar{\rho}H = 0 \qquad \text{(S1)}$$

in Cartesian geometry, and

$$\frac{1}{r^2}\frac{\partial}{\partial r}\left(r^2 k\frac{\partial T}{\partial r}\right) + \bar{\rho}H = 0 \qquad \text{(S2)}$$

in spherical geometry, where T is the temperature, z (in Eq. S1) the depth, r (in Eq. S2) the radius, k the thermal conductivity, $\bar{\rho}$ the density and H the heating rate per unit of mass. Considering that k, $\bar{\rho}$ and H are constant throughout the system, and taking surface and bottom temperatures, T_{surf} and T_{bot}, as boundary conditions, integrations of Eqs. (S1) and (S2) lead to the expressions listed in Table S1 for the temperature and heat flux profiles. Note that in Cartesian geometry, D is the thickness of the domain, and in spherical geometry, R and r_c are the total and core radii, $f = r_c/R$ the ratio between these radii, and $D = (R - r_c)$, again, the thickness of the conductive layer. Expressions for radial profiles of heat flux (also listed in Table S1) are obtained by derivating the radial profiles for temperature with respect to either z in Cartesian geometry, or r in spherical geometry. In this later case, one may recall that the heat flux is defined as the opposite of the temperature derivative with respect to radius.

In the case of the outer shells of icy bodies, the bottom temperature is known from the liquidus at the bottom of the ice shell. Instead of using T_{bot} as boundary condition, one may use the surface heat flux, Φ_{surf}. This surface heat flux is given by

$$\Phi_{surf} = k\frac{\Delta T}{D} + \frac{\bar{\rho}HD}{2} \qquad \text{(S3)}$$

in Cartesian geometry (z = 0), and, noting that $(2 - f - f^2) = (1 - f)(2 + f)$ and $R = D/(1 - f)$, by

$$\Phi_{surf} = k\frac{\Delta T}{D}f + \frac{\bar{\rho}HD}{6}(2 + f)\,, \qquad \text{(S4)}$$

in spherical geometry (r = R). Temperature profiles then write

$$T(z) = T_{surf} + z\frac{\Phi_{surf}}{k} - \frac{\bar{\rho}Hz^2}{2k}\,, \qquad \text{(S5)}$$

in Cartesian geometry, and

$$T(r) = T_{surf} - \frac{\Phi_{surf}}{k}R\left(1 - \frac{R}{r}\right) + \frac{\bar{\rho}HR^2}{6k}\left[2\left(1 - \frac{R}{r}\right) + \left(1 - \frac{r^2}{R^2}\right)\right] \qquad \text{(S6)}$$

in spherical geometry.

S1.2 Application to stagnant lids

Depending on whether the bottom temperature, T_{bot}, or the surface heat flux, Φ_{surf}, is known or easier to access, either expressions in Table S1 or Eqs. (S5) and (S6) may be used to describe temperature profiles within conductive systems or conductive layers. These equations may, in particular be used to infer the thermal profile within the rigid lid that forms at the top of a system animated with stagnant-lid convection (section 3.2), which writes

$$< T >= T_{surf} + z\frac{\Phi_{surf}}{k} - \frac{\bar{\rho}Hz^2}{2k} \quad \text{(S7)}$$

in Cartesian geometry, and

$$< T >= T_{surf} - \frac{\Phi_{surf}}{k}R\left(1-\frac{R}{r}\right) + \frac{\bar{\rho}HR^2}{6k}\left[2\left(1-\frac{R}{r}\right)+\left(1-\frac{r^2}{R^2}\right)\right] \quad \text{(S8)}$$

in spherical geometry. If Φ_{surf} is known, Eqs. (S7) and (S8) can be directly used to determine the temperature profiles within the stagnant lid.

If the thickness of the stagnant lid, d_{lid}, and the temperature at its bottom, T_{lid}, are specified instead of the surface heat flux, expressions given in Table S1 lead to

$$< T >= T_{surf} + \Delta T_{lid}\frac{z}{d_{lid}} + \frac{\rho Hz}{2k}(d_{lid} - z) \quad \text{(S9)}$$

in Cartesian geometry, and

$$< T >= T_{surf} - \Delta T_{lid}\frac{R}{d_{lid}}f_{lid}\left(1-\frac{R}{r}\right) + \frac{\rho HR^2}{6k}\left[f_{lid}(1+f_{lid})\left(1-\frac{R}{r}\right)+\left(1-\frac{r^2}{R^2}\right)\right] \quad \text{(S10)}$$

in spherical geometry, where $\Delta T_{lid} = \left(T_{lid} - T_{surf}\right)$ is the temperature jump across the stagnant lid, and $f_{lid} = (R - d_{lid})/R = 1 - (1-f)\,d_{lid}/D$ the ratio between the radius of its base and the total radius. Numerical simulations of stagnant lid convection give easily access to the surface heat flux, while the average temperature at the bottom of the stagnant lid, T_{lid}, is more difficult to estimate. To calculate the temperature profiles within stagnant lids Eqs. (S7) and (S8) are thus handier than Eqs. (S9) and (S10).

Heat flux equations in Table S1 may further be used to estimate the temperature at the bottom of stagnant lids given the surface heat flux and the lid thickness. In this case, heat flux writes

$$\Phi(z) = k\frac{\Delta T_{lid}}{d_{lid}} + \frac{\bar{\rho}H}{2}(d_{lid} - 2z) \quad \text{(S11)}$$

in Cartesian geometry, and

$$\Phi(r) = k\frac{\Delta T_{lid}}{d_{lid}} f_{lid}\left(\frac{R}{r}\right)^2 + \frac{\bar{\rho}Hr}{3}\left[1 - \frac{f_{lid}(1+f_{lid})}{2}\frac{R^3}{r^3}\right] \tag{S12}$$

in spherical geometry. Taking Eqs. (S11) and (S12) at the surface (z = 0 or r = R), and rearranging the terms, one gets the temperature at the bottom of the lid, $T_{lid} = T_{surf} + \Delta T_{lid}$, as a function of the surface heat flux and stagnant lid thickness, following

$$T_{lid} = T_{surf} + \frac{d_{lid}}{k}\left(\Phi_{surf} - \frac{\bar{\rho}Hd_{lid}}{2}\right) \tag{S13}$$

in Cartesian geometry, and

$$T_{lid} = T_{surf} + \frac{d_{lid}}{kf_{lid}}\left[\Phi_{surf} - \frac{\bar{\rho}HR}{6}(2 - f_{lid} - f_{lid}^2)\right] \tag{S14}$$

in spherical geometry.

S2. Trends in scaling laws for temperature and heat flux

Supplementary Figures S1 and S2 plot the non-dimensional interior temperature, $\tilde{T}_m$, and surface heat flux, $\tilde{\Phi}_{top}$, as a function of the input parameters of numerical simulations and following scaling laws inferred in sections 4.1 and 4.2 of the main article (Eqs. 21 and 23). Input parameters are the surface Rayleigh number, Ra_{surf}, the ratio between the inner and outer radii of the shell, f (with f = 1 for Cartesian geometry), the non-dimensional rate of internal heating, $\widetilde{H}$, and the non-dimensional inverse of the viscous temperature scale, γ, controlling the amplitude of viscosity variations with temperature. The viscosity law follows the Frank-Kamenetskii approximation, implying that γ = ln(Δη), where Δη is the top-to-bottom viscosity ratio. As discussed in sections 4.1 and 4.2, two sets of parameters are needed to explain the results of the simulations, depending on whether the Urey number, Ur, defined by Eq. (12) of the main text, is smaller or larger than 1. This leads to discontinuities for cases where Ur ~ 1.

Figure S1 shows that $\tilde{T}_m$ increases with $\widetilde{H}$, as one would expect, but decreases with increasing Ra_{surf}, while $\widetilde{\Phi}_{top}$ increases monotically with both $\widetilde{H}$ and Ra_{surf}. Interior temperature further decreases as curvature gets larger (*f* decreases). The amplitude of variations in $\tilde{T}_m$ with *f* are rather limited compared to variations of $\tilde{T}_m$ with $\widetilde{H}$, but comparable to those induced by changes in Ra_{surf}. Note that $\widetilde{\Phi}_{top}$ does not depend explicitly on *f* (Eq. 23 of main text), but is nevertheless sensitive to this parameter because the effective Rayleigh number, Ra_{eff} (Eq. 10 of main article) depends on temperature. As a consequence, $\widetilde{\Phi}_{top}$ decreases with increasing curvature, but these variations are relatively limited compared to those induced by changes in Ra_{surf} or $\widetilde{H}$.

The influence of γ on $\tilde{T}_m$ is more complex and depends in particular on the value of $\widetilde{H}$ (plots a and b in Figure S2). For $\widetilde{H} < 1$, $\tilde{T}_m$ monotically increases with γ (and thus with Δη), as observed for stagnant-lid convection with a bottom heated-fluid, i.e., $\widetilde{H} = 0$ (*e.g.*, Moresi and Solomatov, 1995; Deschamps and Sotin, 2000). By contrast, for $\widetilde{H}$ around 1 and higher, $\tilde{T}_m$ first decreases with increasing γ, reaches a minimum value for a value of γ that increases with $\widetilde{H}$, and starts increasing again. It is also interesting to note that the influence of $\widetilde{H}$ becomes smaller as γ increases, *i.e.*, for high values of γ (typically, larger than 25-30), $\tilde{T}_m$ is mostly controlled by γ (and thus by the thermal viscosity contrast) regardless of $\widetilde{H}$. As a consequence, $\tilde{T}_m < 1$ (and thus *Ur* < 1) for such values of γ, and $\tilde{T}_m$ tends asymptotically to 1 as γ goes to infinity. Finally, plots c and d in Figure S2 indicate that $\widetilde{\Phi}_{top}$ increases monotically with γ. As discussed in section 4.2, γ acts on $\widetilde{\Phi}_{top}$ directly, through $1/\gamma^c$ and the exponential term defining Ra_{eff}, and indirectly through $\tilde{T}_m$. Both the $1/\gamma^c$ term in Eq. (23) and, if γ is not too large, the decrease in $\tilde{T}_m$ (and thus in Ra_{eff}) lead to a decrease in $\widetilde{\Phi}_{top}$ as Δη gets larger. However, the exponential term in the definition of Ra_{eff} is dominant, such that for given values of Ra_{surf} and $\widetilde{H}$, $\widetilde{\Phi}_{top}$ increases with Δη. Again, it is worth noting that the influence of $\widetilde{H}$ diminishes as γ gets larger, and that for high viscosity ratios the value of $\widetilde{\Phi}_{top}$ is mostly controlled by the amplitude of these variations.

S3. Modelling of ice shell properties

For applications to Europa, we assumed that the viscosity of ice Ih is described by

$$\eta(T) = \eta_{ref} exp\left[\frac{E}{RT_{ref}}\left(\frac{T_{ref}}{T} - 1\right)\right] \tag{S15}$$

where E is the activation energy, R the ideal gas constant, and η_{ref} the reference viscosity at temperature T_{ref}. The reference viscosity is not well constrained. Close to the melting point, *i.e.* for T_{ref} equal to the liquidus temperature of pure water at the bottom of the ice shell, $T_{H2O,bot}$, a range of values based on polar ice sheet creep is 10^{13}-10^{15} Pa s (Montagnat and Duval, 2000). Here, we considered this parameter as a free parameter and varied it in the range 10^{12}-10^{15} Pa s, extending the range of possible values estimated by Montagnat and Duval (2000). Activation energy is better constrained, with values in the range 49-60 kJ/mol depending on the creep regime (Durham et al., 2010), and around 60 kJ/mol for atomic diffusion (Weertman, 1983). Here, we used E = 60 kJ/mol in all calculations. Under icy moons conditions, ice Ih rheology is likely more complex than the diffusion creep mechanism assumed in Eq. (S15), but it is reasonable to think that the impact of internal heating on ice shell dynamics follows a similar trend for different rheologies.

Following Eq. (22) and the viscosity law (Eq. S15), the viscous temperature scale is

$$\Delta T_v = \frac{RT_m{}^2}{E}, \tag{S16}$$

such that the inverse of the non-dimensional viscous temperature scale, $\gamma = \Delta T/\Delta T_v$, which controls the thermal viscosity contrast, is given by

$$\gamma = \frac{E\Delta T}{RT_m{}^2}, \tag{S17}$$

where $\Delta T = \left(T_{bot} - T_{surf}\right)$ is the top to bottom temperature jump. Still following Eq. (S16), rescaling Eq. (21) of main text gives the interior temperature

$$T_m = T_{bot} - \frac{a_1 R}{E f^{a_2}} {T_m}^2 + (a_1 + a_2 f) \left[\frac{(1+f+f^2)}{3} \frac{\rho_I H D^2}{k_I \Delta T}\right]^{c_3} \frac{\Delta T}{{Ra_{eff}}^{c_4}}, \qquad \text{(S18)}$$

where T_{bot} is the bottom temperature defined as the liquidus of the water + impurities system, H the internal heating rate per mass unit, ρ_{I} and k_{I} the density and thermal conductivity of the ice Ih, respectively, D the thickness of the ice layer, and Ra_{eff} the Rayleigh number calculated with the viscosity temperature T_{m},

$$Ra_{eff} = \frac{\alpha_I \rho_I g \Delta T D^3}{\eta(T_m) \kappa_I}, \qquad \text{(S19)}$$

In Eq. (S19), α_{I} and κ_{I} are the thermal expansion and thermal diffusivity of ice Ih, and $\eta(T_{\mathrm{m}})$ is calculated with Eq. (S15). The values of the parameters a_1, a_2, and c_1 to c_4 are given in section 4.1. Note that parameters c_1 to c_4 have different values depending on whether the Urey ratio (*Ur*, Eq. 12 of main text) is smaller or larger than 1. It is also worth noting that if the sub-surface ocean is composed of pure water, the bottom temperature T_{bot} is equal to the reference temperature defined in the viscosity law (Eq. S15), but is lower than this reference temperature if impurities (*e.g.*, ammonia) are also present (see next paragraph). Equation (S18) does not have analytical solution, and we solved it following a Newton-Raphson zero-search method.

Impurities act as an anti-freeze and may include ammonia (NH_3), methanol (CH_3OH), and salts (*e.g.*, magnesium sulfate, $MgSO_4$). Here, we more specifically considered ammonia, which is predicted to condensate in giant planets environments with amounts up to a few per cent (Mousis et al., 2009; Deschamps et al., 2010). In the case of Europa, magnesium sulfate may further be an important compound of the ocean (Vance et al. 2018). Qualitatively, however, the evolution of the icy bodies is not significantly impacted by the nature of the impurities, but only by their amount. For instance, Vilella et al. (2020) pointed out that the impact of 30 % $MgSO_4$ on the liquidus is equivalent to that of 3.5 % NH_3. On another hand, it should be noted that different compositions may impact physical properties of the ocean, in particular its density. Adding 30 % $MgSO_4$ would increase density by about 150 kg/m^3, while 3.5 % NH_3 would reduce it. Details on the calculation of the water-ammonia system liquidus can be found in Deschamps and Sotin (2001). Practically, we prescribed the initial fraction of ammonia, corresponding to the concentration of ammonia in the initial ocean. The concentration in ammonia then increases as the ocean starts to freeze, since up to the eutectic composition (equal to 32.2 wt% in the case of NH_3), only water ice crystalizes, while impurities are left in the subsurface ocean, whose volume decreases due to the thickening of the outer ice layer. Note that in phase diagrams, concentrations in impurities are usually measured in wt%. For practical reasons, we perform calculations with the volume fraction, which we correct to weight fraction when determining the liquidus, following (in the case of ammonia)

$$x_{NH3}^{wt} = \frac{x_{NH3}^{vol}\rho_{NH3}}{x_{NH3}^{vol}\rho_{NH3} + (1 - x_{NH3}^{vol})\rho_w}, \qquad \text{(S20)}$$

where ρ_w and ρ_{NH3} are the densities of liquid water and ammonia, respectively.

The surface heat flux is obtained by rescaling the heat flux scaling law (Eq. 23 of main text) with the characteristic heat flux, $\Phi_{carac} = k_{ref}\,\Delta T/D$, where k_{ref} is the characteristic thermal conductivity. Most reconstruction of icy bodies thermal evolutions used values of k_{ref} in the range 2.0-3.0 W/m/K, corresponding to the conductivity at the temperature of the well mixed interior or at the bottom of the shell (*e.g.*, Grasset et al., 1996; Tobie et al., 2003; Běhounková et al., 2010). Here, we fixed k_{ref} to 2.6 W/m/K (Grasset and Sotin, 1996). Interestingly, in the case of Europa, this value leads to ice shell properties and thermal evolution very close to those obtained with temperature-dependent thermal conductivity (Deschamps, 2021). Accounting for the shell's curvature, measured with the ratio between the inner and outer radii, *f*, the basal and surface heat fluxes write

$$\Phi_{surf} = \Phi_{carac}\widetilde{\Phi}_{top} \qquad \text{(S21)}$$

and $$\Phi_{bot} = \Phi_{carac}\widetilde{\Phi}_{top}/f^2\,. \qquad \text{(S22)}$$

Note that this formulation is slightly different from that used in Deschamps (2021), where the non-dimensional convective heat flux ($\widetilde{\Phi}_{conv}$) was inferred from 3D-Cartesian calculations and a correction for spherical geometry was assumed, leading to $\Phi_{surf} = f\Phi_{carac}\widetilde{\Phi}_{conv}$ and $\Phi_{bot} = \Phi_{carac}\widetilde{\Phi}_{conv}/f$. Because the curvature of outer ice layers of large icy bodies remains large (typically, f > 0.7), this difference only triggers small to moderate effects on the calculations of ice shell properties and thermal evolution. Note that if the surface heat flux is lower than the conductive characteristic heat flux, Φ_{carac}, the system is not animated by convection and transfers heat by conduction. This occurs, for instance, if the ice shell is too thin or, in the case of a sub-surface ocean containing impurities, too thick. In this later case, the temperature at the bottom of the shell is much lower than in the case of a pure water ocean. As a result, reference and interior viscosities are higher, decreasing the vigor of convection or even shutting off convection (Deschamps and Sotin, 2001).

As discussed in main text, two sets of parameters for Eq. (23) may be used, depending on whether the bottom heat flux, Φ_{bot}, is positive (Ur < 1) or negative (Ur > 1). The threshold (non-dimensional) internal heating is given by Eq. (25) of main text, and may be used as a criteria to decide which set of parameters to use. Here, instead, we used a simpler procedure, which accounts for the fact that temperature and heat flux scalings are not continuous at Ur = 1. First, we calculate the internal temperature T_m (Eq. S18) and the surface heat flux, Φ_{surf}, assuming parameter values for Ur < 1. If the corresponding Φ_{bot} (calculated with Eq. (11) of main text) is negative, we re-evaluate T_m and Φ_{surf}, but with parameter values for Ur > 1. If the resulting Φ_{bot} is positive again, we set arbitrarily its value to zero, and recalculate Φ_{surf} and T_m accordingly.

To calculate the thickness of the stagnant lid, Deschamps (2021) assumed that the temperature at the bottom of the lid is well described by $T_{lid} = 2T_m - T_{bot}$, and then deduced d_{lid} from the expression of the conductive temperature profile within the lid. However, the relationship between T_{lid} and T_m assumes that temperature jump in the bottom and top thermal boundary layers (excluding the stagnant lid) are equal, which is not valid for mixed-heating convection. Here, instead, we estimated the thickness of the stagnant lid by rescaling Eq. (26) of the main article, leading to

$$d_{lid} = \frac{a_{lid}\gamma^c}{{Ra_{eff}}^b} D \,, \tag{S23}$$

where γ and Ra_{eff} are given by Eqs. (S17) and (S19), respectively, the constant a_{lid} is equal to 0.633 for $Ur < 1$ and 0.667 for $Ur > 1$, $b = 0.27$, and $c = 1.21$. The temperature at the bottom of the stagnant lid can then be calculated using Eq. (S14).

S4. Thermal evolution

The present day radial structure of icy bodies may be estimated from appropriate thermal evolution modelling. Here, we followed the approach of Grasset and Sotin (1996), which calculates the evolution of ice layers thicknesses based on an energy balance accounting for the production of heat in the silicate core, the cooling of the ocean, and the crystallization of ice shells. Europa is not large enough to host high pressure ices, such that the inner radius of the outer ice Ih shell, r_{bot}, can be calculated by solving the energy conservation equation at the boundary between this shell and the sub-surface ocean. Energy conservation at this boundary then writes

$$\frac{dr_{bot}}{dt}\left[\rho_w C_w \left(-\frac{\partial T_{ad}}{\partial r} + \frac{\partial T_{bot}}{\partial r}\right)\frac{({r_{bot}}^3 - {r_c}^3)}{3} - \rho_I L_I {r_{bot}}^2\right] = {r_{bot}}^2 \Phi_{bot} - {r_c}^2 \Phi_c \tag{S24}$$

where t is time, T_{bot} and Φ_{bot} are the temperature and heat flux at the bottom of the ice layer, given by the liquidus of the ocean and by Eq. (S22), respectively, r_c is the core radius, Φ_c the heat flux at the top of the core, ρ_w and C_w the liquid water density and heat capacity, ρ_I and L_I the density and latent heat of fusion of ice Ih, respectively, and T_{ad}, the adiabatic temperature in the ocean, given by

$$T_{ad}(r) = T_{bot}(r_{bot})\left[1 - \frac{\alpha_w}{\rho_w c_w}\rho_I g(r - r_{bot})\right], \qquad \text{(S25)}$$

with α_w being the thermal expansion of liquid water. Within the silicate core, heat is assumed to be produced by the decay of 4 radiogenic elements, ^{40}K, ^{232}Th, ^{235}U, and ^{238}U. The heat flux at the top of the core is then calculated following Kirk and Stevenson (1987) by

$$\Phi_c = 2\sqrt{\frac{\kappa_c t}{\pi}}\rho_c \sum_{i=1}^{4} C_{0,i} H_i \frac{[1-\exp(-\lambda_i t)]}{\lambda_i t}, \qquad \text{(S26)}$$

where κ_c and ρ_c are the thermal diffusivity and density of the silicate core, and the subscript *i* refers to the 4 radiogenic elements, whose properties are listed in Table S2. We solved Eq. (S24) up to t = 4.55 Gyr using an adaptative stepsize control Runge-Kutta method (Press et al., 1992), and assuming an initial ice Ih thickness equal to 10 km together with the material and physical properties listed in Table 3 of the main text. Again, because the reference viscosity η_{ref} is a sensitive parameter but is poorly constrained, we performed calculations for values of η_{ref} in the range 10^{12}-10^{15} Pa s, corresponding to an extended range of the values estimated by Montagnat and Duval (2000).

References

Běhounková, M., Tobie, G., Choblet, G., & Čadek, O. (2010). Coupling mantle convection and tidal dissipation : Applications to Enceladus and terrestrial planets, *J. Geophys. Res. Planets*, *115*, doi: 10.1029/2009JE003564.

Davaille, A., & Jaupart, C. (1993). Transient high-Rayleigh-number thermal convection with large viscosity variations. *J. Fluid Mech.*, *253*, 141-166.

Deschamps, F. (2021). Stagnant lid convection with temperature-dependent thermal conductivity and the thermal evolution of icy worlds, *Geophys. J. Int.*, *224*, 1870-1890.

Deschamps, F., & Sotin, C. (2000). Inversion of two-dimensional numerical convection experiments for a fluid with a strongly temperature-dependent viscosity. *Geophys. J. Int.*, *143,* 204-218.

Deschamps, F. & Sotin, C. (2001). Thermal convection in the outer shell of large icy satellites, *J. Geophys. Res.*, *106*, 5107-5121.

Deschamps, F., Mousis, O., Sanchez-Valle, C. & Lunine, J.I. (2010). The role of methanol on the crystallization of Titan's primordial ocean. *Astrophys. J.*, *724,* 887-894.

Durham, W.B., Prieto-Ballesteros, O., Goldsby, D.L. & Kargel, J.S. (2010). Rheological and thermal properties of icy minerals, *Space Sci. Rev.*, *153*, 273-298.

Grasset, O. & Sotin, C. (1996). The cooling rate of a liquid shell in Titan's interior, *Icarus*, *123*, 101-112.

Kirk, R.L. & Stevenson, D.J. (1987). Thermal evolution of a differentiated Ganymede and implications for surface features, *Icarus*, *69*, 91-134.

Montagnat, M. & Duval, P. (2000). Rate controlling processes in the creep of polar ice, influence of grain boundary migration associated with recrystallization, *Earth Planet. Sci. Lett.*, *183*, 179-186.

Moresi, L.-N. & Solomatov, V.S. (1995). Numerical investigation of 2D convection with extremely large viscosity variations, *Phys. Fluids*, **7**, 2154-2162.

Mousis, O., Lunine, J. I., Thomas, C., Pasek, M., Marboeuf, U., Alibert, Y., Ballenegger, V., Cordier, D., Ellinger, Y., Pauzat, F., & Picaud, S. (2009). Clathration of volatiles in the Solar nebula and implications for the origin of Titan's atmosphere. *The Astrophysical Journal*, *691*, 1780-1786.

Press, W.H., Flannery, B.P. Teukolsky, S.A. & Vetterling, W.T. (1992). Numerical Recipes, 2nd edtion, Cambridge University Press, pp. 701-725.

Tobie, G., Choblet, G. & Sotin, C. (2003). Tidally heated convection: constraints on Europa's ice shell thickness, *J. Geophys. Res.*, *108*, doi: 10.1029/2003JE002099.

Vilella, K., Choblet, G., Tsao, W.E. & Deschamps, F. (2020). Tidally heated convection and the occurrence of melting in icy satellites: application to Europa, *J. Geophys. Res. Planets*, *125*, e2019JE006248, doi: 10.1029/2019JE006248.

Weertman, J. (1983). Creep deformation of ice, *Ann. Rev. Earth Planet. Sci.*, *11*, 215-240.

Table S1. Relationships for radial profiles of temperature and heat flux for a conductive mixed-heated system.

Quantity	Geometry	Expression
Temperature	Cartesian	$T_{surf} + \Delta T \frac{z}{D} + \frac{\bar{\rho} H z}{2k}(D - z)$
-	Spherical	$T_{surf} - \Delta T \frac{R}{D} f\left(1 - \frac{R}{r}\right) + \frac{\bar{\rho} H R^2}{6k}\left[f(1+f)\left(1 - \frac{R}{r}\right) + \left(1 - \frac{r^2}{R^2}\right)\right]$
Heat flux	Cartesian	$k\frac{\Delta T}{D} + \frac{\bar{\rho} H}{2}(D - 2z)$
-	Spherical	$k\frac{\Delta T}{D} f\left(\frac{R}{r}\right)^2 + \frac{\bar{\rho} H r}{3}\left[1 - \frac{f(1+f)}{2}\frac{R^3}{r^3}\right]$

$\Delta T = (T_{bot} - T_{surf})$ is the bottom-to-top temperature jump, where T_{surf} and T_{bot} are the surface and bottom temperature and D is the thickness of the shell. In Cartesian geometry, z is depth, and in spherical geometry, r is radius, R the total radius, and $f = r_{bot}/R$ the ratio between the inner and outer radii of the shell. k is the thermal conductivity, H the rate of internal heating, and $\bar{\rho}$ the average density, which are here all considered as being constant.

Table S2. Properties of long-lived radioactive isotopes.

Element	Decay constant, λ (1/yr)	Heat release, H (W/kg)	Initial abundance, C_0 (ppb)
^{40}K	5.4279×10^{-10}	2.917×10^{-5}	738.0
^{232}Th	4.9405×10^{-11}	2.638×10^{-5}	38.7
^{235}U	9.8485×10^{-10}	5.687×10^{-4}	5.4
^{238}U	1.5514×10^{-10}	9.465×10^{-5}	19.9

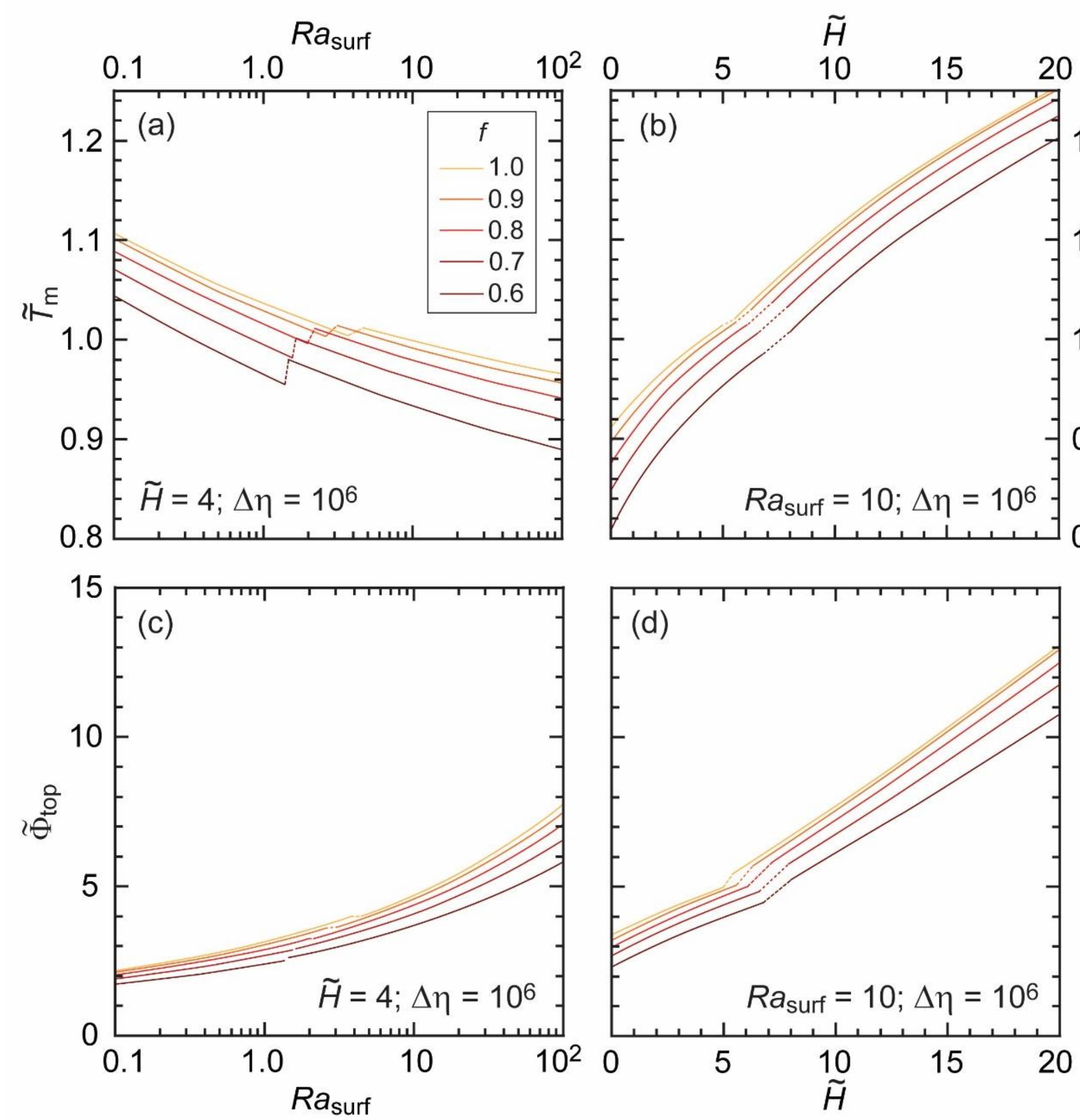

Figure S1. Non-dimensional interior temperature $\tilde{T}_m$ deduced from Eq. (21) (top row) and surface heat flux $\widetilde{\Phi}_{top}$ calculated from Eq. (23) (bottom row) as a function of the surface Rayleigh number Ra_{surf} (left column) and non-dimensional rate of internal heating $\widetilde{H}$ (right column), and for several values of the ratio between the inner and outer shell radii f (color code; f = 1 indicates Cartesian geometry). Two sets of parameters for Eqs. (21) and (23) are used, depending on whether the Urey ratio (*Ur*, Eq. 12) is smaller or larger than 1 (see main article), leading to discontinuities at *Ur* ~ 1. For calculations as a function of Ra_{surf} (left column), $\widetilde{H}$ is set to 4, and for calculations as a function of $\widetilde{H}$ (right column), Ra_{surf} is equal to 10. In all cases, the surface top-to-bottom viscosity ratio is fixed to 10^6.

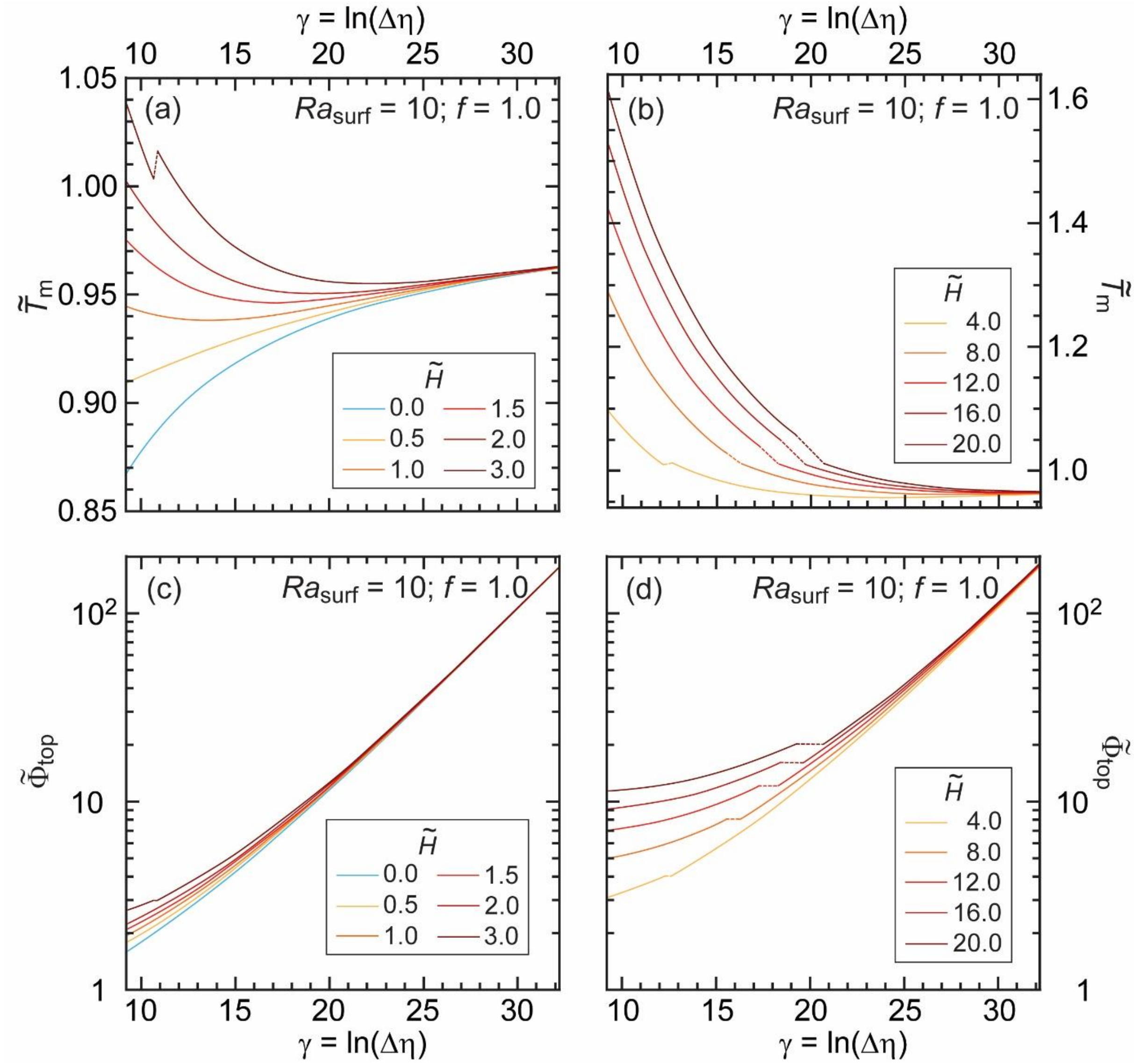

Figure S2. Non-dimensional interior temperature $\tilde{T}_m$ deduced from Eq. (21) (top row) and surface heat flux $\tilde{\Phi}_{top}$ calculated from Eq. (23) (bottom row) as a function inverse of the non-dimensional viscous temperature scale, $\gamma = \Delta T / \Delta T_v$ (see main text), and for several values of the non-dimensional rate of internal heating (color code). The viscosity is described by a Frank-Kamenetskii law (Eq. 7), such that γ is equal to the logarithm of the top-to-bottom viscosity ratio. Two sets of parameters for Eqs. (21) and (23) are used, depending on whether the Urey ratio (*Ur*, Eq. 12) is smaller or larger than 1 (see main article) and leading to discontinuities at *Ur* ~ 1. In all cases, the surface Rayleigh number is equal to 10, and geometry is Cartesian (*f* = 1).

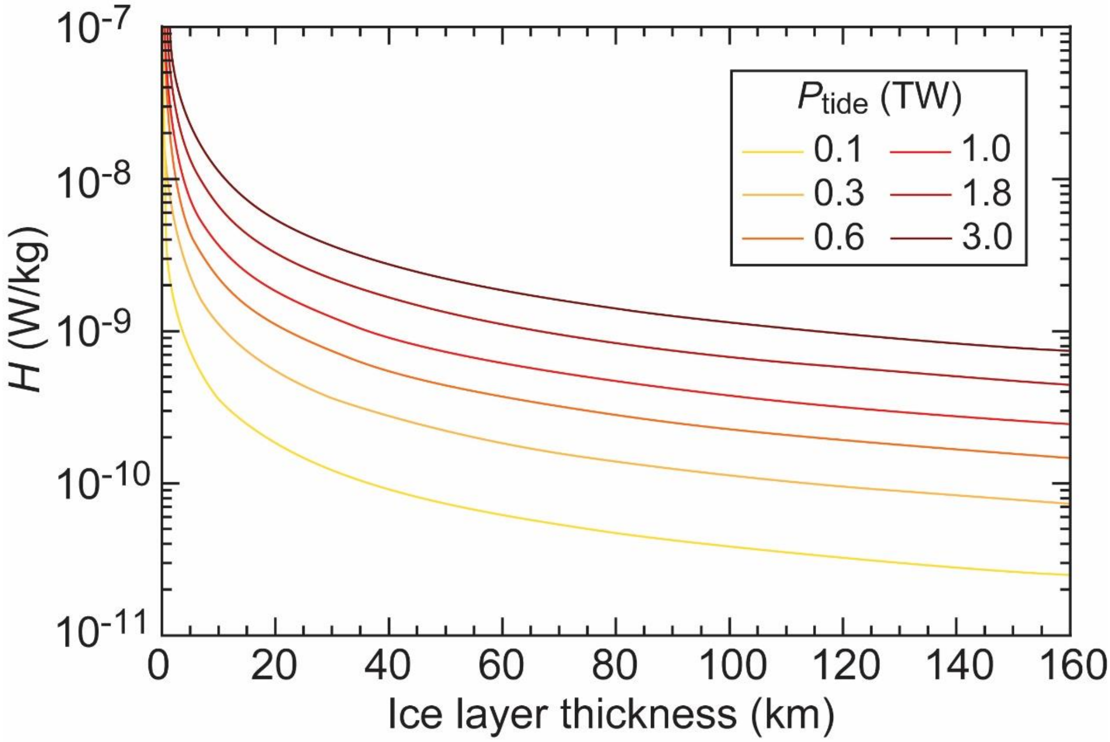

Figure S3. Rate of internal heating per mass unit as a function of the ice shell thickness and for several values of the total power dissipated in the ice layer (color code). The density of the ice shell is ρ_I = 920 kg/m^3.

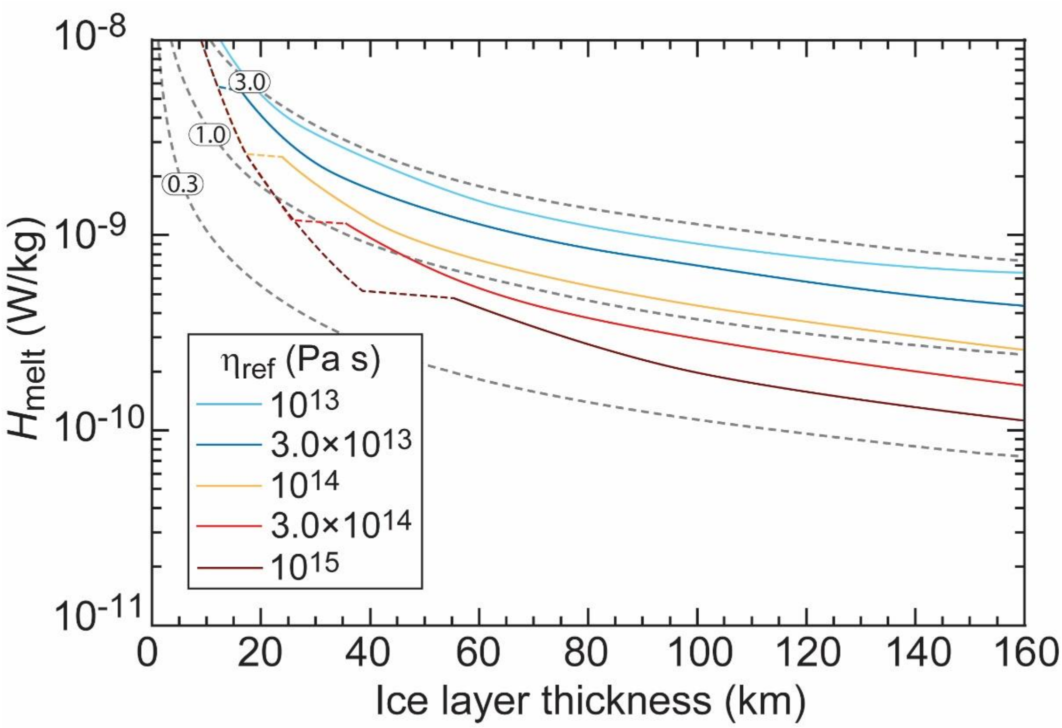

Figure S4. Critical values of internal heating for partial melting of the ice shell, H_{melt}, as a function of the ice shell thickness and for different values of the reference viscosity, η_{ref}. Calculations are made with the properties of Europa (Table 3) and assuming a sub-surface ocean composed of pure water. Dashed parts of the curves indicate that the system is not animated by convection, based on the observation that the convective heat flux is smaller than the conductive heat flux. The grey dashed curves represent the heating rate for three values of the total power dissipated within the ice shell (values in TW indicated on each curve).

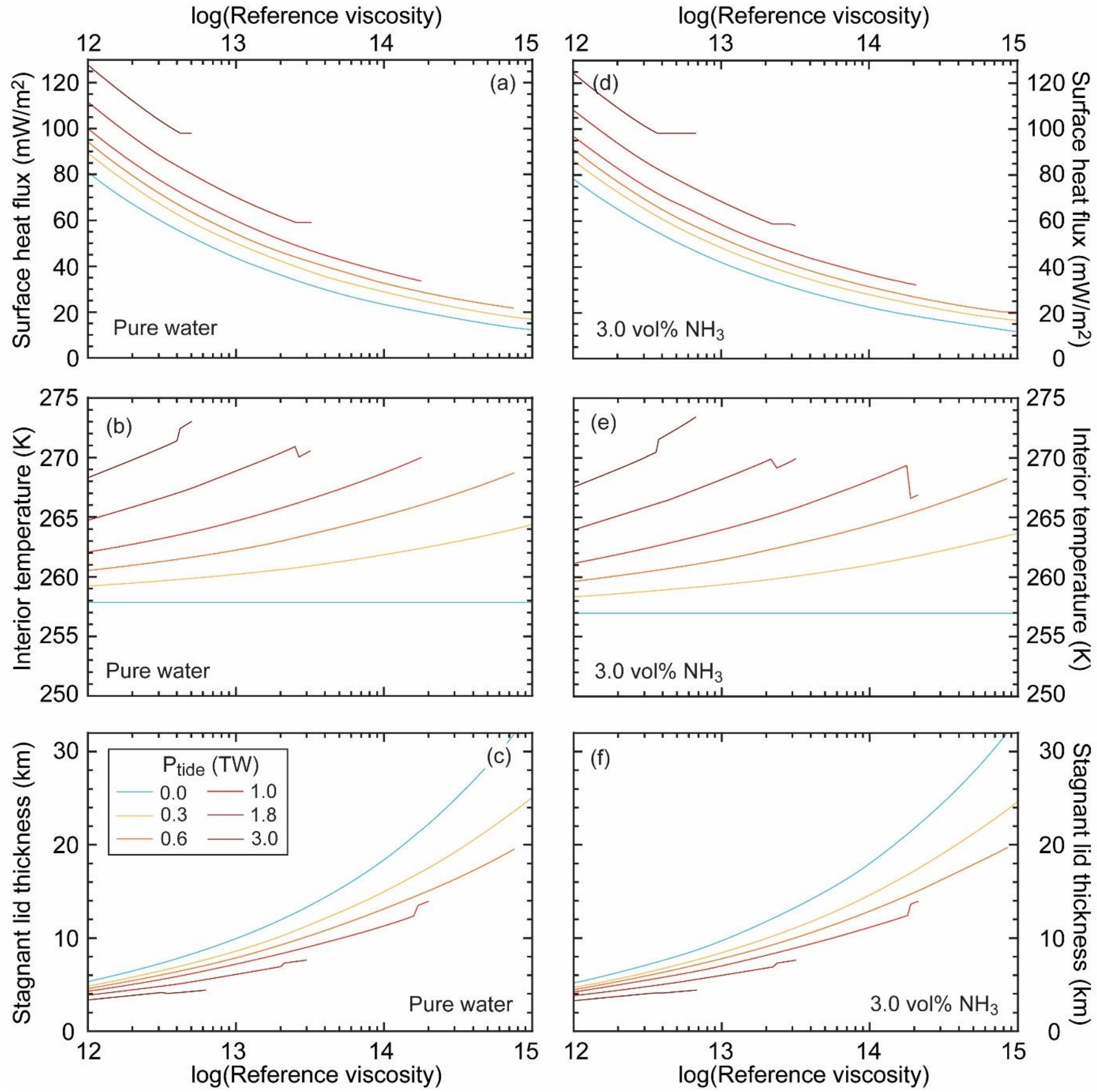

Figure S5. Properties of a 40 km thick ice Ih shell as a function of the reference viscosity, η_{ref}, and for several values of the total power dissipated in the ice layer (color code). (a) and (d) Surface heat flux. (b) and (e) Interior temperature. (c) and (f) Stagnant lid thickness. Physical properties used for calculations are listed in Table 3, and two initial compositions of the ocean are considered, pure water (left column), and an initial mix of water and 3.0 vol% ammonia (right column). Curves interruptions indicate that the average interior temperature is larger than the liquidus of pure water at that depth. Two regimes occur depending on whether the Urey ratio (*Ur*, Eq. 12) is smaller or larger than 1, leading to discontinuities at *Ur* ~ 1.

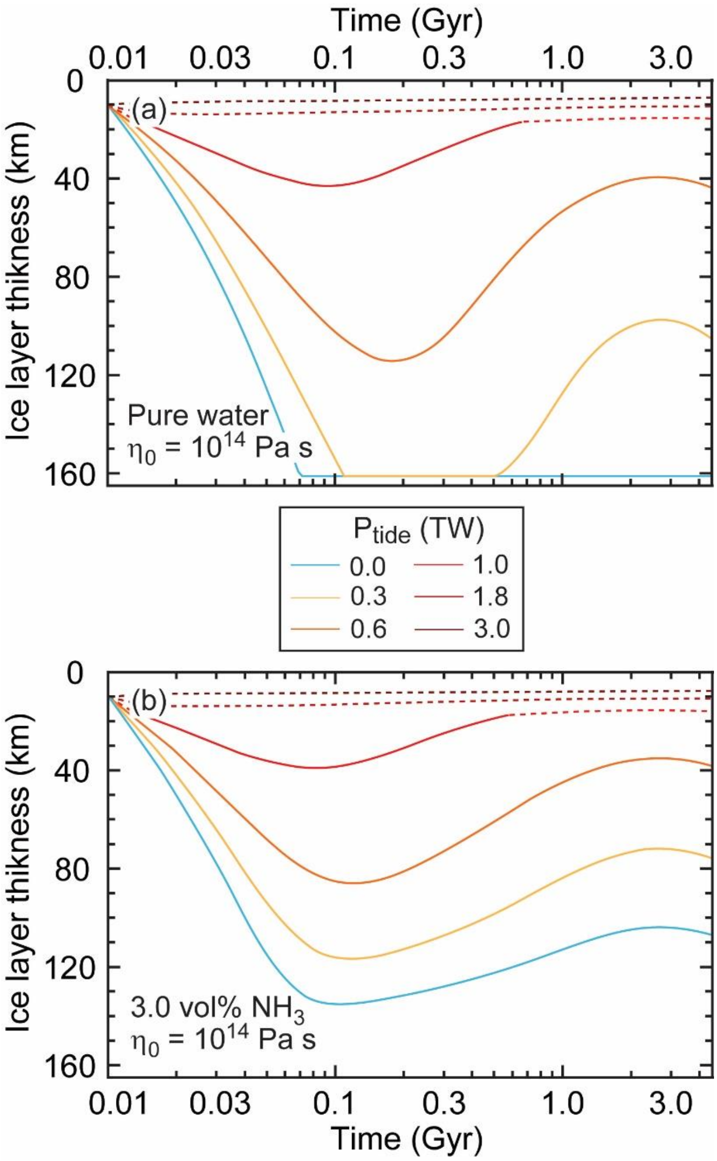

Figure S6. Evolution of the ice shell thickness as a function of time for reference viscosity η_{ref} = 10^{14} Pa s and several values of the total power dissipated in the ice layer (color code). The composition of the ocean is (a) pure water, or (b) an initial mix of water and 3.0 vol% ammonia. Note the logarithmic scale for the time axis.

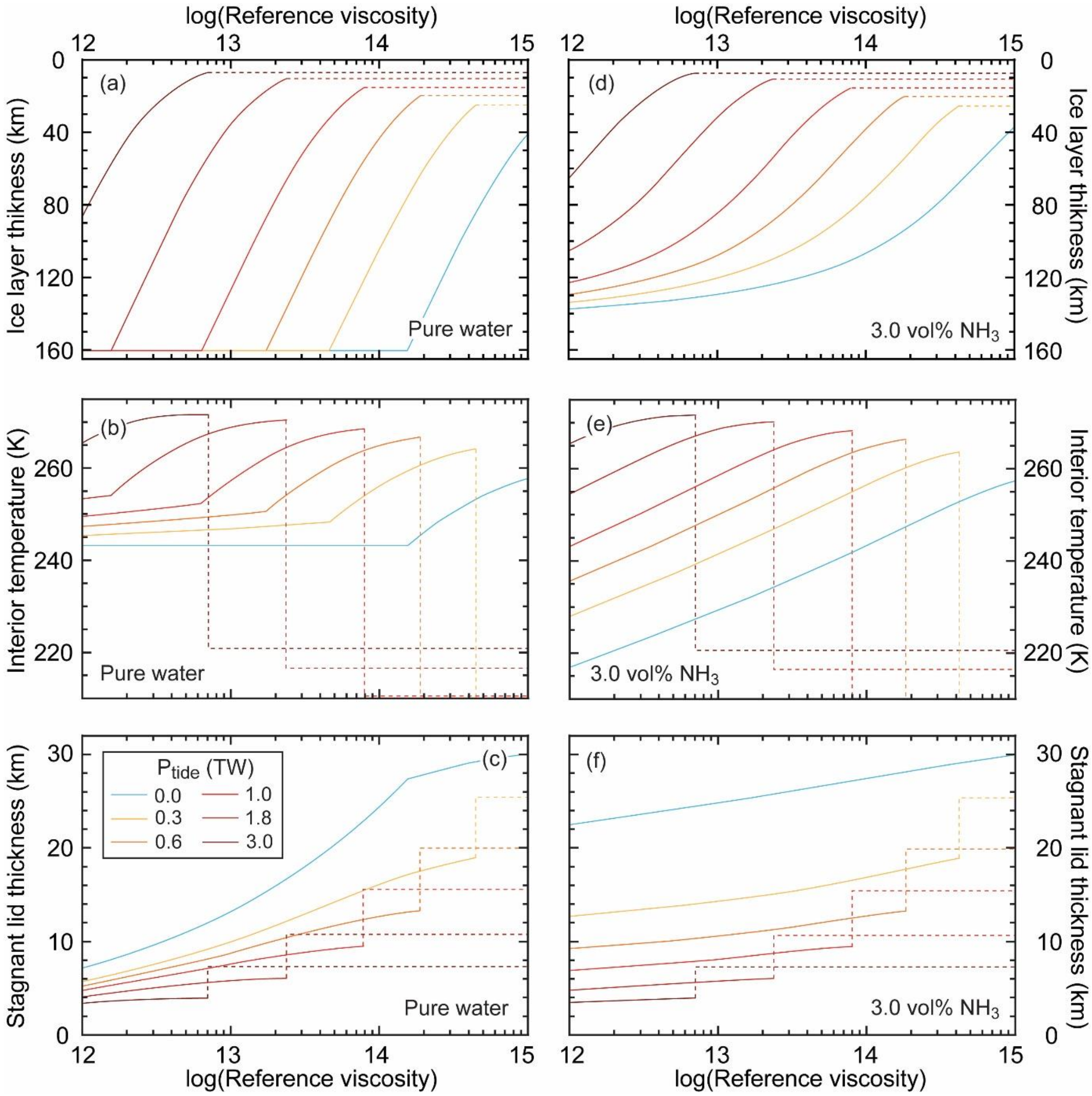

Figure S7. Properties of Europa's outer ice shell at t = 4.55 Gyr as a function of the reference viscosity, η_{ref}, and for several values of the total power dissipated in the ice layer (color code). (a) and (d) Ice shell thickness. (b) and (e) Interior temperature. (c) and (f) Stagnant lid thickness. Physical properties used for calculations are listed in Table 3, and two initial compositions of the ocean are considered, pure water (left column), and an initial mix of water and 3.0 vol% ammonia (right column). Dashed parts of the curves indicate that the system is not animated by convection.